

Controls on melt migration and extraction at the ultraslow Southwest Indian Ridge 10°–16°E

Laurent G. J. Montési,¹ Mark D. Behn,² Laura B. Hebert,¹ Jian Lin,² and Jennifer L. Barry^{3,4}

Received 25 January 2011; revised 23 June 2011; accepted 7 July 2011; published 4 October 2011.

[1] Crustal thickness variations at the ultraslow spreading 10–16°E region of the Southwest Indian Ridge are used to constrain melt migration processes. In the study area, ridge morphology correlates with the obliquity of the ridge axis with respect to the spreading direction. A long oblique “supersegment”, nearly devoid of magmatism, is flanked at either end by robust magmatic centers (Joseph Mayes Seamount and Narrowgate segment) of much lesser obliquity. Plate-driven mantle flow and temperature structure are calculated in 3-D based on the observed ridge segmentation. Melt extraction is assumed to occur in three steps: (1) vertical migration out of the melting region, (2) focusing along an inclined permeability barrier, and (3) extraction when the melt enters a region shallower than ~35 km within 5 km of the ridge axis. No crust is predicted in our model along the oblique supersegment. The formation of Joseph Mayes Seamount is consistent with an on-axis melt anomaly induced by the local orthogonal spreading. The crustal thickness anomaly at Narrowgate results from melt extracted at a tectonic damage zone as it travels along the axis toward regions of lesser obliquity. Orthogonal spreading enhances the Narrowgate crustal thickness anomaly but is not necessary for it. The lack of a residual mantle Bouguer gravity high along the oblique supersegment can be explained by deep serpentinization of the upper mantle permissible by the thermal structure of this ridge segment. Buoyancy-driven upwelling and/or mantle heterogeneities are not required to explain the extreme focusing of melt in the study area.

Citation: Montési, L. G. J., M. D. Behn, L. B. Hebert, J. Lin, and J. L. Barry (2011), Controls on melt migration and extraction at the ultraslow Southwest Indian Ridge 10°–16°E, *J. Geophys. Res.*, 116, B10102, doi:10.1029/2011JB008259.

1. Introduction

[2] Plate tectonics requires that plate boundaries be significantly weaker than plate interiors [Sacks *et al.*, 1968; Bercovici, 2003]. This includes divergent plate boundaries [Mammerickx and Sandwell, 1986; Norrell, 1991; Hirth *et al.*, 1998; Mitchell *et al.*, 2011], where weakening may be related to advective thinning of the lithosphere and the presence of melts in the mantle [Tackley, 2000]. As these two weakening processes are related to the divergence rate, it is possible that there is a minimum spreading rate necessary for plate boundaries, and therefore plate tectonics, to exist [Sleep, 2000]. The slowest ridges on Earth, ultraslow spreading centers, probe the limits of what it means to be a

plate boundary. We study in detail a specific example of an ultraslow spreading center, the 10–16°E area of the Southwest Indian Ridge (Figure 1), to constrain the principles of melt migration there, which can later be used to constrain the distribution of melt at depth and the resistance of the ridge to far-field plate motions.

[3] Ultraslow spreading ridges differ from “regular” mid-ocean ridges, and have been classified as “a new type of plate boundary” [Dick *et al.*, 2003]. Ultraslow ridges rarely feature transform discontinuities. Instead, their axes may be strongly oblique to the direction of spreading, reducing the effective spreading rate and significantly thickening the near-surface thermal boundary layer (TBL) [Montési and Behn, 2007]. Ultraslow ridges often feature long amagmatic segments, vast areas of the seafloor that are essentially devoid of magmatic products [Dick *et al.*, 2003; Michael *et al.*, 2003; Cannat *et al.*, 2006]. However, even at these ultraslow spreading rates, scaling analyses for the sub-ridge thermal structure predict that melt is produced by adiabatic decompression melting [Montési and Behn, 2007]. Furthermore, these amagmatic segments are punctuated by large isolated volcanic centers, where the crust is likely thicker than standard oceanic crust [Dick *et al.*, 2003; Michael *et al.*, 2003; Sauter *et al.*, 2001, 2004; Standish *et al.*, 2008].

¹Department of Geology, University of Maryland, College Park, Maryland, USA.

²Department of Geology and Geophysics, Woods Hole Oceanographic Institution, Woods Hole, Massachusetts, USA.

³Swarthmore College, Swarthmore, Pennsylvania, USA.

⁴Now at Computer Science and Artificial Intelligence Laboratory, Massachusetts Institute of Technology, Cambridge, Massachusetts, USA.

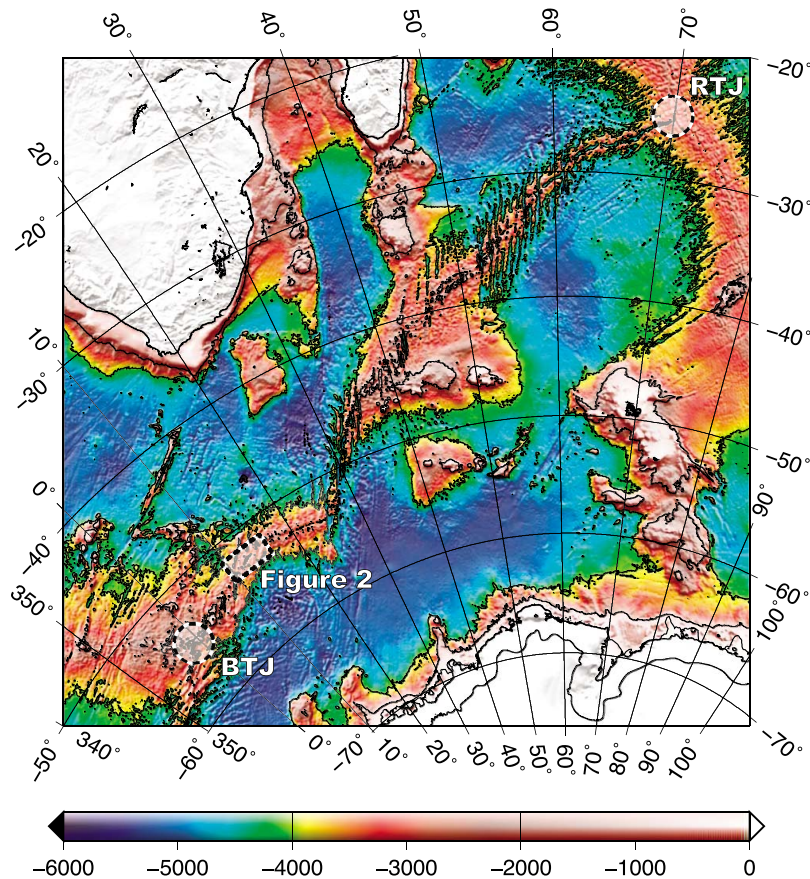


Figure 1. Map of the entire Southwest Indian Ridge from the Bouvet Triple Junction (BTJ) to the Rodrigues Triple Junction (RTJ). Opening direction is roughly up-down on this map (Oblique Mercator projection centered at 30°E, 50°S). The study area is highlighted by the dashed box labeled Figure 2. Bathymetric data from ETOPO2v2.

[4] Thus, it appears that it is melt extraction, not melt production, that is inefficient at ultraslow spreading ridges, with the magma produced beneath the amagmatic segments transported tens of km to localized volcanic centers [Standish *et al.*, 2008]. In this study, we develop a quantitative model for melt migration and extraction at ultraslow ridges, which explains this focusing as the consequence of ridge segmentation.

2. Magmatic Variability Along the Southwest Indian Ridge 10–16°E

[5] The 10–16°E area of the Southwest Indian Ridge (SWIR) is an excellent example of an oblique ultraslow spreading ridge that displays punctuated volcanism along its axis (Figure 2). Located between South Africa and Antarctica, the SWIR is a slow-spreading ridge, opening within the study area at a half rate $V_p = 7.0$ mm/yr [DeMets *et al.*, 1994]. Locally, the SWIR reaches very slow effective spreading rates due to the high obliquity between the ridge axis and the overall spreading direction [Dick *et al.*, 2003]. Here, we define obliquity as the angle θ between the opening direction and the normal to the ridge axis. Thus, a standard, orthogonal, spreading center has an obliquity of 0°, while a transform zone has an obliquity of 90°.

[6] The greatest obliquity in the 10–16°E region of the SWIR (Figure 2) is found along the 200 km-long Oblique Supersegment #2 (OS2), where $\theta \sim 60^\circ$. The effective spreading rate, defined as $V_e = V_p \cos \theta$ decreases to 3.5 mm/yr in this area, even slower than at the Gakkel Ridge—the archetypal ultraslow ridge [Dick *et al.*, 2003; Montési and Behn, 2007]. The OS2 segment displays the characteristics of ultraslow spreading centers: a continuous, wide, and deep rift axis, with high relief along its flanks. Large mantle blocks are exhumed at the ridge axis, basalts and gabbro are only rarely recovered (Figure 2a), and no magnetic lineations are present, implying that the OS2 segment is essentially devoid of crust [Dick *et al.*, 2003; Standish *et al.*, 2008].

[7] By contrast, large bathymetric highs mark the ends of the OS2 oblique supersegment [Dick *et al.*, 2003]. To the west, Joseph Mayes Seamount (JMS), a well-defined on-axis seamount, reaches water depths of less than 2000 m, while the rift axis within OS2 is as deep as 4700 m. The shape of JMS is sigmoidal, spanning roughly 15 km of the ridge axis. To the east, the OS2 segment merges with the 25-km-long orthogonal Narrowgate segment, which is flanked off-axis by anomalously shallow seafloor. Narrowgate features abundant volcanism with lava characterized by high K_2O content and K/Ti ratio [Le Roex *et al.*, 1992; Standish *et al.*, 2008]. In addition, young lavas have been recovered 10 km off-axis

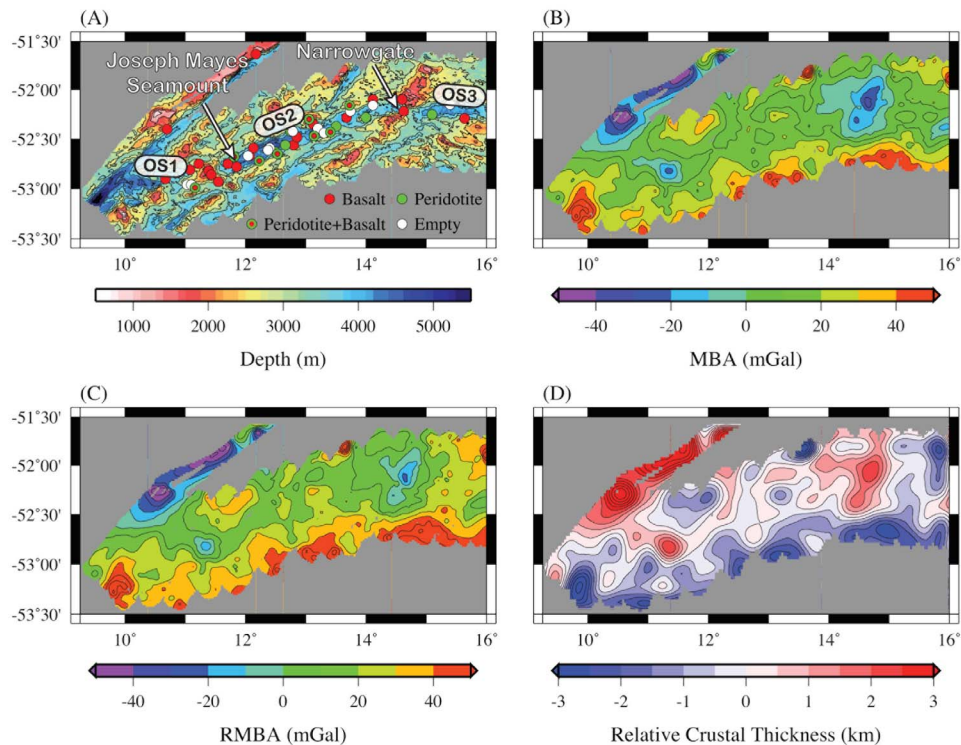


Figure 2. (a) Bathymetry, (b) mantle Bouguer gravity anomaly (MBA), (c) residual mantle Bouguer gravity anomaly (RMBA), and (d) gravity-derived crustal thickness variations in the study area. Bathymetry and MBA data are taken from *Dick et al.* [2003]. Colored circles in Figure 2a show dredge locations and lithologies from *Standish et al.* [2008]. RMBA is calculated based on the thermal model calculated for Configuration A in Table 1. The segments discussed in the text are indicated on Figure 2a, following the definition of *Montési and Behn* [2007]. Note that many of the dredges labeled “basalt” along OS2 returned only a small quantity of rocks [*Standish, 2005*].

from the Narrowgate segment, indicating that crustal accretion is not limited to the rift valley floor [*Standish and Sims, 2010*]. Both JMS and Narrowgate are characterized by well-defined magnetic lineations and negative mantle Bouguer gravity anomalies (Figure 2b), indicating a thickened crustal layer [*Dick et al., 2003*]. West of JMS and east of Narrowgate, the Oblique Segments #1 and 3 (OS1 and OS3) have intermediate obliquity and again display a deep and wide rift axis, albeit with more abundant volcanism than along the OS2 oblique supersegment (Figure 2a).

[8] To first order, the effective spreading rate of a ridge segment controls its axial thermal structure [*Montési and Behn, 2007*]. As the effective spreading rate decreases, cooling of the lithosphere becomes more efficient. This results in a thickening of the TBL, which in turn truncates the melting column near the surface [*Bown and White, 1994; White et al., 2001*]. However, decompression melting is expected even at the slowest effective spreading rates along the SWIR [*Montési and Behn, 2007*]. Thus, one possible explanation for the paucity of volcanism at the OS2 supersegment is that low-degree melts produced beneath high-obliquity segments are channeled to the adjacent magmatic centers [*Montési and Behn, 2007; Standish et al., 2008*]. This is consistent with the composition of the Narrowgate basalts, which require an unusually high proportion of sil-

ica-enriched low degree melts [*Le Roex et al., 1992; Standish et al., 2008*].

3. Permeability Barriers as a Mechanism for Focusing Melts

[9] It has long been recognized that pressure gradients arising solely from solid mantle flow are insufficient to focus melts generated off-axis to the ridge axis [*Phipps Morgan, 1987; Spiegelman and McKenzie, 1987*]. *Sparks and Parmentier* [1991] proposed an alternative model in which lateral melt transport occurs primarily along a permeability barrier that forms at the base of the TBL. As melts rise toward the surface, they encounter the TBL, where they begin to cool and crystallize. Rapid crystallization fills pore space and decreases permeability [*Korenaga and Kelemen, 1997; Kelemen and Aharonov, 1998*], especially if the connectivity of melt networks decrease [*Zhu and Hirth, 2003*]. The zone of reduced permeability acts as a barrier to melt propagation below which melt accumulates and forms a decompaction channel [*Sparks and Parmentier, 1991; Spiegelman, 1993*]. As the TBL is less thick on-axis than off-axis, the permeability barrier is inclined, and melt buoyancy resolved along the barrier induces lateral melt migration toward the axis, where it later pools and erupts. The presence of a permeability barrier at the base of

Table 1. Definition of Model Segments

Interpretation	Segment Endpoints	Segment Length	Obliquity
<i>Configuration A (Preferred)</i>			
Orthogonal segment	[0,100] to [200,200]	100 km	0°
Shaka transform	[100,100] to [200,410]	210 km	90°
OS1a	[100,147] to [410,430]	51 km	23°
OS1b	[147,170] to [430,470]	46 km	60°
Joseph Mayes Seamount	[170,185] to [470,470]	15 km	0°
OS2	[185,300] to [470,660]	222 km	59°
Narrowgate	[300,325] to [660,660]	25 km	0°
OS3	[325,400] to [660,715]	93 km	36°
Orthogonal supersegment	[400,510] to [715,725]	110 km	5°
<i>Configuration B</i>			
Orthogonal segment	[0,100] to [200,200]	100 km	0°
Shaka transform	[100,100] to [200,410]	210 km	90°
OS1a	[100,147] to [410,430]	51 km	23°
OS1b	[147,177.5] to [430,470]	50 km	52°
OS2	[177.5,312.5] to [470,660]	233 km	55°
OS3	[312.5,400] to [660,715]	103 km	32°
Orthogonal supersegment	[400,510] to [715,725]	110 km	5°
<i>Configuration C</i>			
Orthogonal segment	[0,100] to [200,200]	100 km	0°
Shaka transform	[100,100] to [200,410]	210 km	90°
Oblique supersegment	[100,400] to [410,715]	428 km	46°
Orthogonal supersegment	[400,510] to [715,725]	110 km	5°

the TBL can also explain deep pooling of melt and metasomatism of the mantle under mid-ocean ridges [Cannat, 1996; Warren and Shimizu, 2010; Shaw et al., 2010], as well as instances of off-axis magmatism [Garmany, 1989; Sims et al., 2003; Nedimović et al., 2005; Canales et al., 2009].

[10] Melt focusing in the presence of a permeability barrier has been studied in 2-D [Sparks and Parmentier, 1991; Spiegelman, 1993; Ghods and Arkani-Hamed, 2000; Katz, 2008, 2010] and 3-D [Sparks et al., 1993; Magde et al., 1997; Gregg et al., 2009; Weatherley and Katz, 2010; Hebert and Montési, 2011] numerical models. In 3-D, ridge segmentation induces melt focusing not only toward but also along the axis. For example, Magde and Sparks [1997] showed that at the slow-spreading Mid-Atlantic Ridge, melt migration along a permeability barrier generates more realistic variations in crustal thickness than do diapiric instabilities. Here, we explore whether a similar scenario applies to the punctuated volcanism observed along the slow/ultraslow SWIR 10°–16°E area.

[11] Strong melt focusing by migration along a permeability barrier requires that the slope of the TBL is sufficient to drive melt migration. Although there are no transform offsets in the 10°–16°E region of the SWIR, the observed variations in segment obliquity imply variations in TBL thickness by a factor of two [Montési and Behn, 2007], with the thinnest TBL beneath JMS and Narrowgate. In this study, we (1) calculate the 3-D thermal structure of the mantle and the geometry of the permeability barrier, and (2) solve for melt trajectories and expected crustal variations throughout the study area. We also evaluate the critical slope of the TBL required for melt migration and the maximum lithospheric thickness through which melt can be extracted to the surface. Our numerical results are compared with geologic observations and a new gravity-derived along-axis profile of crustal thickness (Figure 2d).

[12] We consider only passive mantle flow, driven by plate divergence, ignoring buoyancy-driven flow. Although

scaling relations (Appendix A) indicate that buoyancy becomes important at slow and ultraslow spreading center [Lin and Phipps Morgan, 1992], our assumption of purely plate-driven flow is justified *a posteriori* by the success of this model at reproducing crustal thickness variations for certain parameters relating to near-axis melt extraction. Nevertheless, future work should seek to obtain a similar agreement with the observations using a model where mantle buoyancy is not neglected.

4. Mantle Flow Model

4.1. Model Description

[13] Mantle flow and thermal structure are solved using the COMSOL Multiphysics® 3.4 Finite Element Software. We start by defining the geometry of the ridge axis in map view within a 510 km × 900 km computation domain. Our region of interest is limited by the Shaka transform (10°E) and the transition to the orthogonal supersegment (16°E), which displays a typical slow-spreading ridge morphology with continuous volcanism and short non-transform offsets [Grindlay et al., 1998; Dick et al., 2003; Standish et al., 2008]. Table 1 describes the ridge geometry adopted in our preferred model (Configuration A) and in two simpler cases (Configurations B and C), which are used to illustrate the key aspects of the segmentation pattern required for the success of our model.

[14] The map view geometry is meshed using triangles for maximum flexibility. Maximum element size is reduced to 20 km near the axis for increased resolution. The mesh and geometry are extruded vertically to a depth of 100 km, with layer spacing varying from 6 km at the surface to 13 km at the bottom of the model. The result is a 3-D mesh of vertical triangular prisms (Figure 3). The flow field is solved for using the “Navier-Stokes” application in COMSOL Multiphysics® with variable viscosity, and temperature is computed using the “Conduction and Advection” COMSOL

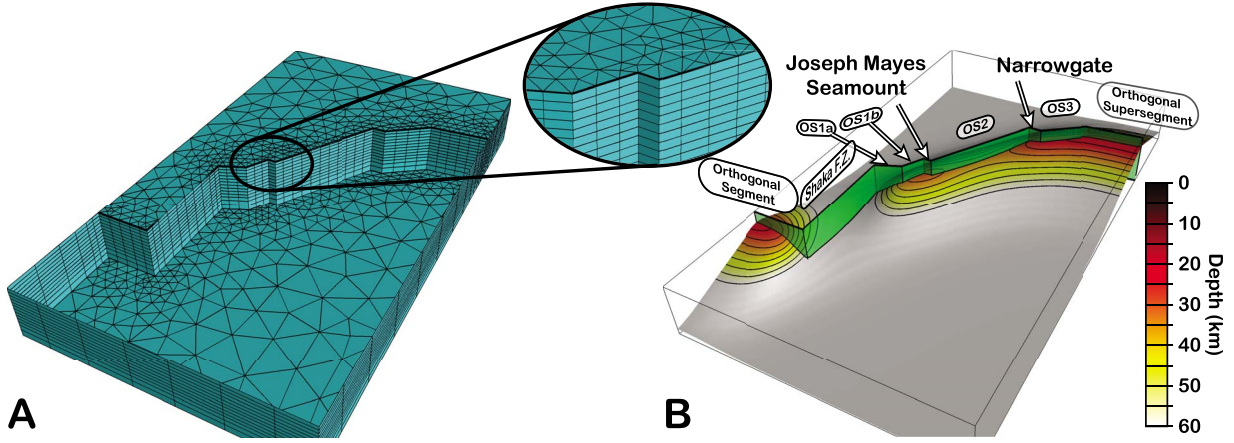


Figure 3. Visualization of (a) the finite element mesh used in our model and (b) the permeability barrier (color coded with depth with 5 km contour interval) with the downward projection of the ridge axis (green surface). The Antarctic plate is made transparent in Figure 3a to better display the depth discretization. Figure 3b also indicates which geological feature each segment of the idealized plate boundary represents.

Multiphysics® application. Interpolation is quadratic in temperature and velocity and linear in pressure. Thus, there are at least two nodes even in the smallest segment (Figure 3). As the thickness of the TBL is predicted to be 25 km or more in the study area [Montési and Behn, 2007], the temperature field is expected to be smooth over length scales of 10 km at the depth of the TBL. Thus, the mesh resolution used here is sufficient to capture the physical phenomena addressed in this study.

[15] Following Behn *et al.* [2007] and Roland *et al.* [2010], we adopt a temperature and stress-dependent viscosity, where the stress is limited by a depth-dependent yield criterion

$$\eta = \min(\eta_T, \eta_Y) \quad (1)$$

$$\eta_T = \eta_0 \exp \left[\frac{Q}{R} \left(\frac{1}{T} - \frac{1}{T_m} \right) \right] \quad (2)$$

$$\eta_Y = \frac{C_0 - \mu \rho g z}{\sqrt{2} \dot{\epsilon}_{II}} \quad (3)$$

where z is depth, $\dot{\epsilon}_{II}$ is the second invariant of the strain rate tensor, and temperature is in Kelvin. All the other parameters in these relations are given in Table 2. Viscosity is restricted to be between a minimum of $\eta_m = \eta_0$ and a maximum of η_M .

[16] All model variables and parameters are compiled in Table 2, which gives also the default values or range of values considered in this study, when appropriate.

[17] A uniform velocity is imparted to the surface of each plate and symmetry is imposed on the model edges parallel to the spreading direction. Free flow (no traction) is imposed on all other boundaries. As a working hypothesis, buoyancy is neglected throughout this study. Temperature is fixed to 0°C at the surface and $T_M = 1375^\circ\text{C}$ at the bottom of the model. Side boundaries are set to convective flux only, implying no diffusive heat transfer across these boundaries.

[18] The flow solution for the non-linear, temperature- and stress-dependent viscosity model is solved using the continuation method [Chen and Morgan, 1990; Behn *et al.*, 2007; Katz, 2008] using the isoviscous flow field and temperature solution as an initial guess. The maximum viscosity, η_M , is initially set to η_0 but is ramped up pro-

gressively to the final value of $10,000\eta_0$. The model is assumed to be in steady state and is solved iteratively using the default solver provided by COMSOL Multiphysics®.

4.2. Temperature Solution

[19] As expected, our 3-D thermal model results in a thicker TBL beneath segments with greater obliquity (Figure 4). Both the Shaka transform (90° obliquity) and the oblique supersegment (59° obliquity) have a marked effect on the thermal structure due to their length and extreme obliquity. By contrast, the relatively short orthogonal segments at JMS and Narrowgate have only subtle effects on the temperature field. The overall effect of our 3-D thermal calculation is to smooth temperature variations along the axis, resulting in a thinning of the TBL beneath JMS and Narrowgate that is less than that predicted from simply scaling by the effective spreading rate [Montési and Behn, 2007]. For example, based solely on the change in V_e , the TBL is predicted to thin from 40 to 20 km between the OS2 and Narrowgate segments, respectively. However, because the transition in the TBL associated with the difference in obliquity between the OS2 and OS3 segments is smoothed over ~ 100 km of ridge axis, almost no thinning of the TBL is observed beneath Narrowgate (Figure 4).

4.3. Predicted On-Axis Melting

[20] Based on the calculated thermal structure, melting is expected everywhere at depth along the plate boundary except beneath the Shaka transform (Figure 4). We adopt a linear melting function

$$F = \frac{T + G_a z - T_S}{\Delta T_{sl}}, \quad \text{with} \quad (4)$$

$$T_S = 1120 + 4.3092 z - 0.0052224 z^2 \quad (5)$$

where T_S is the melting temperature, in °C, taken from Hirschmann [2000], z is the depth, in km, and G_a is an adiabatic gradient we superimpose to our model (Table 2). ΔT_{sl} represents the temperature difference between the solidus and liquidus, and includes a correction for latent heat of fusion [Reid and Jackson, 1981]. We calibrated ΔT_{sl} to produce roughly 6 km of crust in the orthogonal

Table 2. Definitions of Model Parameters and Variables

Name	Symbol	Equation	Units
Variables			
Coordinates	x, y, z		km
Mantle velocity	v_x, v_y, v_z		km
Temperature	T		°C
Solidus temperature	T_s	equation (5)	°C
Temperature at the permeability barrier	T_k	equation (7)	°C
Depth at the permeability barrier	z_k		km
Slope of the permeability barrier	S	equation (8)	km/km
Equilibrium melt fraction	F	equation (4)	No dimension
On-axis melt production	P_a	equation (6)	km/km
Effective viscosity	η	equation (1)	Pa.s
Effective viscosity (ductile process)	η_T	equation (2)	Pa.s
Effective viscosity (brittle process)	η_Y	equation (3)	Pa.s
Second invariant of the strain rate tensor	$\dot{\epsilon}_{II}$		s ⁻¹
Melt productivity	p	equation (9)	s ⁻¹
Melt flux to the permeability	f	equation (10)	km/s
Average F of melt flux to the permeability	F_a^f	equation (13)	No dimension
Length of ridge spanned by a swath	L^s		km
Crustal thickness produced by a swath	H^s	equation (12))	km
Average F of melt collected in a swath	F_a^s	equation (13)	No dimension
<hr/>			
Name	Symbol	Default Value (Range)	Units
Parameters			
Model domain		510 × 900 × 100	km ³
Spreading half rate	V_p	7.07	mm/yr
Thermal diffusivity	κ	1	mm ² /s
Mantle temperature	T_m	1375 (1350–1435)	°C
Adiabatic gradient	G_a	0.6475	°C/km
Temperature difference between solidus and liquidus	ΔT_{sl}	900	°C
Reference viscosity	η_0	10 ¹⁹	Pa.s
Maximum viscosity	η_M	10 ²³	Pa.s
Minimum viscosity	η_m	10 ¹⁹	Pa.s
Activation energy	Q	250	kJ/mol
Gas constant	R	8.314	kJ/mol/K
Cohesion	C_0	10	MPa
Coefficient of friction	μ	0.6	No dimension
Density	ρ	3300	kg/m ³
Gravity	g	9.8	m/s ²
Critical melt fraction	F_c	0.01	No dimension
Extraction depth	Z_t	35 (30–40)	km
Lower extraction depth	Z_b	60	km
Shunting distance	D_e	5 (none–10)	km
Critical slope	S_t	0 (0–0.3)	km/km
Lower critical slope	S_b	S_t	km/km

supersegment near 16°E in our preferred model. More realistic melting models would be nonlinear and feature a change in melting rate at the point of pyroxene exhaustion [e.g., *Kinzler and Grove, 1992; Katz et al., 2003*]. However, pyroxene exhaustion is not achieved at the low degrees of melting of our model. Neglecting nonlinear effects probably contributes to the high value of ΔT_{sl} required to produce 6 km of crust along the orthogonal supersegment. Lower mean extents of melting could also be achieved by including hydrous melting [*Asimow and Langmuir, 2003*] and/or melting of a fertile component such as eclogite.

[21] To evaluate the amount of melt produced beneath the ridge axis, we calculate the crustal production rate associated with on-axis melting, P_a (Figure 4, top)

$$P_a = \int_{z_b}^0 \frac{\partial F}{\partial z} \frac{v_z}{2V_p} dz \quad (6)$$

where v_z is the upwelling velocity from the flow solution and z_b is the depth of the model domain. P_a would mimic

crustal thickness if all melting occurred on axis or over a cross-section normal to the axis of constant area. This calculation shows that JMS is associated with an on-axis melting anomaly, with a clear maximum in on-axis crustal production (Figure 4, top). By contrast, Narrowgate is not associated with an on-axis melting anomaly and appears only as a second-order variation in the transition from the OS2 to OS3 segments. Thus, as we discuss in the following section, along-axis perturbations in melt production rate alone are not able to explain the observed variations in crustal thickness along the 10–16°E region of the SWIR.

4.4. Comparison to Gravity-Derived Crustal Thickness Variations

[22] Gravity data from the study area indicate pronounced crustal thickness variations. Mantle Bouguer gravity anomalies (MBA, Figure 2b) were calculated assuming a 5 km thick crust layer [*Dick et al., 2003*]. To correct for variations in density associated with mantle thermal structure, we calculated a residual mantle Bouguer anomaly (RMBA) using

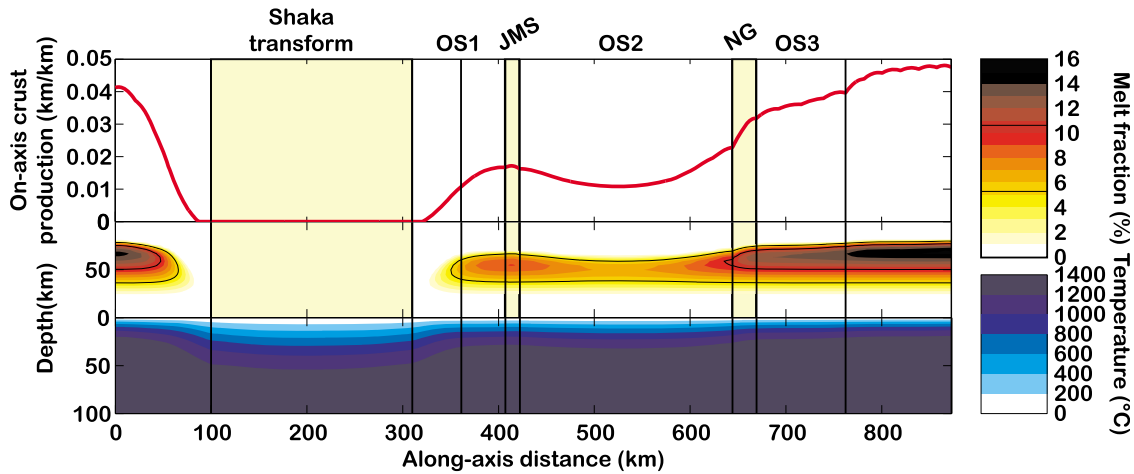


Figure 4. (top) The relative crustal variations that arise solely from melt production beneath the axis. (middle) Equilibrium melt fraction and (bottom) temperature immediately below the ridge axis. In this figure as in Figures 7, 8, and 12, the fields are plotted against a coordinate that follows the plate boundary, including transform and oblique segments. The vertical black bars show the limits of the segments defined in Table 1.

the 3-D temperature field from our model, a mantle density of 3300 kg/m^3 , and a coefficient of thermal expansion of $1 \times 10^{-5} \text{ }^\circ\text{C}^{-1}$ (Figure 2c). This correction reduces the magnitude of the negative MBA anomalies over JMS and Narrowgate by $\sim 10 \text{ mGal}$ relative to the adjacent oblique segments. Finally, RMBA is converted into crustal thickness variations following the method of *Kuo and Forsyth* [1988] assuming a density contrast between the crust and mantle of 450 kg/m^3 and a reference crustal thickness of 5 km (Figure 2d). We stress that the gravity-derived crustal thicknesses calculated here place no bounds on the absolute crustal thickness and can only be used to interpret relative changes along the ridge axis.

[23] The resulting crustal thickness variations feature local anomalies beneath JMS and Narrowgate of $\sim 2\text{--}3 \text{ km}$ relative to the adjacent amagmatic segments. While the JMS anomaly is primarily centered on the ridge axis, increased crustal thickness associated with Narrowgate extends off-axis, particularly to the north. Thick crust is also predicted along the bathymetric high adjacent to the northern extension of the Shaka fracture zone, probably the result of interaction with the Bouvet hot spot. Remarkably, in spite of geological evidence, the OS2 supersegment is not associated with strongly reduced crustal thickness. A possible explanation for the lack of apparent crustal thinning is the presence of low-density, serpentinized mantle beneath the OS2 supersegment, as we will discuss in section 6.3.

[24] The melting anomaly predicted at JMS based on our thermal model (Figure 4) is more subdued and has a wider along-axis extent than the gravity-derived crustal thickness anomaly (Figure 2d). In addition, the model does not feature a melting anomaly beneath Narrowgate capable of producing the observed crustal thickness variations. Thus, for the case of purely plate-driven flow, the large crustal thickness anomalies at Narrowgate and, to some extent, at JMS must be the result of efficient melt focusing. In the following section, we present a model of melt migration along a permeability barrier that reproduces the observed

variations in crustal thickness in the $10\text{--}16^\circ\text{E}$ region of the SWIR.

5. Melting and Melt Migration

5.1. Model Description

5.1.1. Definition of the Permeability Barrier

[25] We assume that melt focusing takes place along a permeability barrier formed at the base of the lithosphere [*Sparks and Parmentier*, 1991]. *Kelemen and Aharonov* [1998] proposed that the barrier develops at the multiple saturation point of plagioclase and pyroxene, which they determined to be at 1240°C at the base of the crust. *Montési and Behn* [2007] took into account the pressure dependence of plagioclase saturation, determined experimentally by *Yang et al.* [1996] and proposed that the temperature of the barrier should be

$$T_k = 1240 + 1.9z \quad (7)$$

with z the depth in km and T_k in $^\circ\text{C}$.

[26] The surface defined by equation (7) is visualized in Figure 3b and Figure 5. The barrier is clearly influenced by ridge obliquity, reaching depths of 20 and 47 km beneath the orthogonal and oblique supersegments, respectively. JMS is associated with a local minimum in permeability barrier depth of 33 km, but no such local minimum is observed beneath Narrowgate at the transition from the moderately oblique OS3 segment to the highly oblique OS2 supersegment (Figure 3b).

[27] *Hebert and Montési* [2010] used a full thermodynamic formalism to compute the crystallization rate of melts produced at various spreading rates and off-axis distances as they enter the TBL. They confirmed that the maximum crystallization rate, where the barrier is most likely to develop, is associated with plagioclase \pm clinopyroxene saturation and that equation (7) captures the conditions of this crystallization maximum to within 10°C in the mantle. However, *Hebert and Montési* [2010] also showed that the

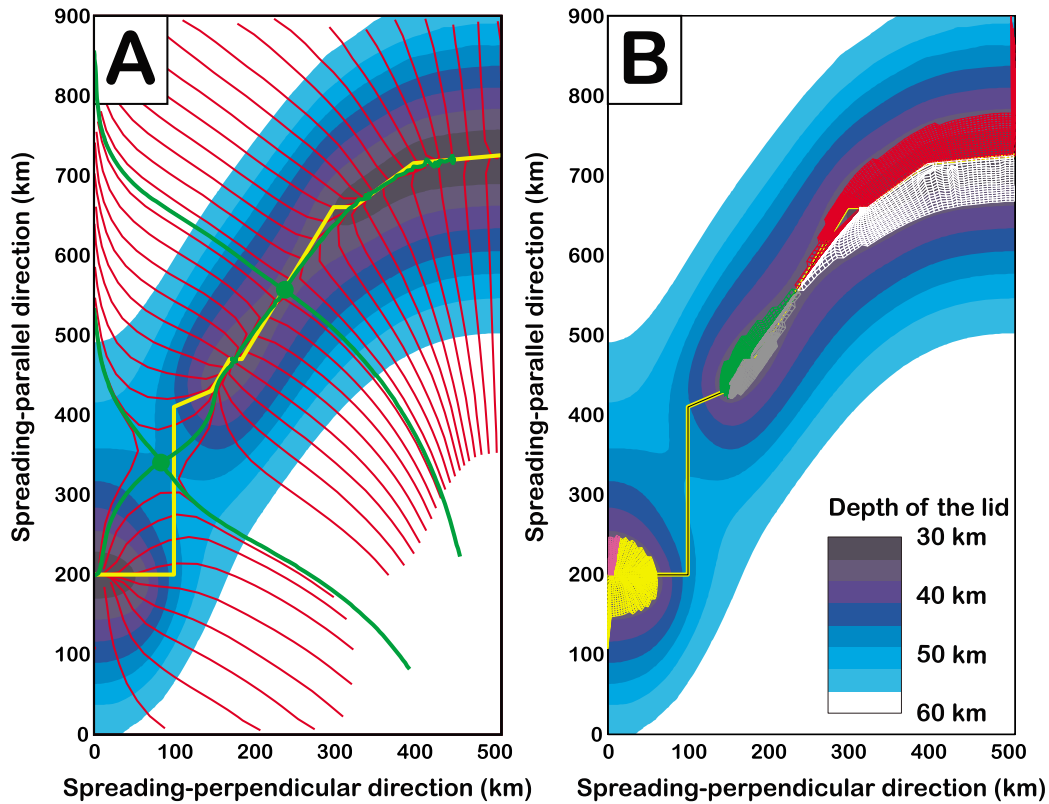


Figure 5. Map of the depth to the permeability barrier for our preferred model. Superposed on the barrier are (a) melt trajectories (red), the plate boundary (yellow) and lines that divide the permeability barrier into regions distinct domains for computation purpose (green). (b) The detailed tessellation of the barrier used for computing crustal thickness, color-coded by computation domain. Actual calculations use five times as many lines as shown in Figure 5a.

crystallization rate at slow spreading may not be sufficient for a strong permeability barrier to form. Mechanisms not yet quantified, such as melt-rock reaction or a temperature/crystallization feedback, may be necessary to produce a barrier. As we do not yet know how these mechanisms would affect the temperature/depth relation of the barrier, we chose to follow equation (7), recognizing that it will probably need to be modified in the light of future studies.

[28] Other studies have chosen to associate the barrier with the solidus or with the crystallization of a binary system with a refractory and a fusible component [Sparks and Parmentier, 1991; Magde and Sparks, 1997; Ghods and Arkani-Hamed, 2000; Katz, 2008; Gregg et al., 2009; Weatherley and Katz, 2010]. In a multicomponent system, as Hebert and Montési [2010] used to constrain equation (7), crystallization is not the reverse of melting, and therefore, the permeability barrier could form at a different depth than the solidus. However, in practice, T_k is not very different from the solidus and we verified that alternative definitions of the permeability barrier have only a minor effect on our results.

[29] The latent heats of fusion and crystallization, which are neglected in this study, would affect the temperature field and the shape of the barrier [Katz, 2008]. In a subduction zone setting, where the overriding plate is stationary, continued magma flux may have a strong effect on the shape of the permeability barrier [England and Katz, 2010].

This effect is likely less important at mid-ocean ridges, where the plate is continuously advected away from the region of active melting.

5.1.2. Melt Migration

[30] Following the concepts first proposed by Sparks and Parmentier [1991], we assume that melt initially travels upward out of the region where it forms and collects in a decompaction channel at the base of the permeability barrier. Zhu et al. [2011] showed that melt remains well-connected even at porosities as low as 2%, justifying efficient melt migration in the melting region (Appendix A). Then, melt migrates upward along the permeability barrier in the direction of maximum slope [Magde and Sparks, 1997]. It is necessary to implement limits to melt migration unless all the melt collects at a small number of points along the ridge axis. In particular, we take into account the possibility of a zone of rapid melt extraction around the plate boundary.

[31] Figure 6 illustrates schematically the various domains of our melt migration and extraction models. In the *focusing zone*, the slope of the barrier is sufficient for melt to travel upward along the barrier. Here, slope is a non-dimensional ratio defined as

$$S = dz_k/dl \quad (8)$$

where z_k is the depth of the permeability barrier and l is a curvilinear coordinate along the path taken by the melt.

[32] Rigorously, melt migration in the focusing zone is driven by pressure gradients in the decompaction channel that develops at the base of the permeability barrier [Sparks and Parmentier, 1991; Spiegelman, 1993; Katz, 2008]. In practice, we compute the path taken by a particle as it moves along the barrier in the direction of maximum slope, defining a *melt line*. Selected melt lines for our preferred model are displayed in Figure 5a.

[33] The focusing zone ends when the slope of the barrier is less than a critical value. We define different critical slopes at shallow and deep levels, S_t and S_b , to account for the possibility that the permeability within the decompaction channel varies with depth. Further, crystallization at great enough depth may be sufficiently slow that a permeability barrier does not develop [Hebert and Montési, 2010]. Therefore, the focusing zone is also limited by a critical depth Z_b .

[34] Melt that collects at the permeability barrier at greater depths than the focusing zone does not migrate along the barrier. It will cool, crystallize and metasomatize the mantle at fairly great depth. We find that the details of the deeper extent of the focusing zone do not affect significantly our results. Therefore, all the models presented here use $S_b = S_t$ and $Z_b = 60$ km. However, the deeper limits to melt extraction may play an important role in controlling crustal thickness at fast spreading rates [Gregg et al., 2009; Hebert and Montési, 2010].

[35] Near the surface, it is necessary to implement another limit on the extent of melt migration along the barrier. Specifically, under certain conditions, melt will penetrate through permeability barrier, exit the decompaction channel, and follow easy pathways through the lithosphere to the surface [Ghods and Arkani-Hamed, 2000; Katz, 2008]. A well-developed magma plumbing system may provide these easy pathways. Volcanism observed in association with faulting [Fornari et al., 1989; Hékinian et al., 1992; Macdonald et al., 1996; Perfit et al., 1996; Tucholke et al., 2008] and evidence of melt impregnation in shear zones at ophiolites [Kelemen and Dick, 1995; Kaczmarek and Müntener, 2008] indicates that faults may act also as easy pathways for melt extraction. We assume that the region of easy melt transport, which we term the *shunting zone* by analogy with the shunting process in electric circuits, extends to distance D_e from the plate boundary and to a depth Z_t .

[36] Melt lines are truncated at the point where they exit the focusing zone. A straight line joins the truncation point to the nearest point along the plate boundary. Together, this segment and the truncated melt line form a *melt trajectory* (Figure 6).

[37] If the truncation point is shallower than Z_b , all the melt collected along the melt trajectory in the focusing zone and along the truncation segment is extracted at the ridge. We associate this melt to the nearest point along the plate boundary (Figure 6), where it contributes to the crustal thickness.

[38] If the truncation point is deeper than Z_b , the melt collected along the melt trajectory in the focusing zone stalls at the truncation point and crystallizes in-situ to refertilize the ambient mantle. Refertilized peridotites have been reported in many environments, including slow and ultraslow spreading centers and ophiolites [Nicolas and Prinzhofer, 1983; Seyler et al., 2001; Brunelli et al., 2006; Le Roux et al., 2007; Warren et al., 2009; Dick et al., 2010]. Melt generated beneath the truncation segment would also refertilize the lithosphere at locations where the truncation segment is deeper than Z_t , but it could be extracted if it is generated close enough to the

ridge axis, where the permeability barrier along the truncation segment may be shallower than Z_t . Extracted melt contributes to the crustal thickness at the end of the melt trajectory. We also keep track of any melt that refertilizes the lithosphere (here termed *cryptic crust*) along the melt trajectory.

[39] Given our extraction scheme, four main classes of melt trajectories are possible (Figure 6). In trajectory A, melt follows the melt line until its slope is less than S_t . As this happens at a depth shallower than Z_t , all the melt is extracted at the axis (red circle). Only deep melt serves to refertilize the mantle. In trajectory B, melt follows the melt line until it enters the shunting zone. At that point, the melt no longer follows the permeability barrier but is extracted at the closest point along the plate boundary. In trajectory C, melt follows once again the melt line until its slope is less than S_t , but as this happens at a depth greater than Z_t , all the melt collected up to this point refertilizes the lithosphere (green circle). Melt generated closer to the axis along trajectory C will either refertilize the lithosphere without focusing (green line) or be extracted at the axis (red line and circle) if the melt trajectory is shallower than Z_t . Trajectory D is similar to trajectory C but never shallower than Z_t . Therefore, none of the melt is extracted. Note that in this case, the melt trajectory passes underneath the shunting zone.

[40] To compute crustal thickness, we consider swaths of the permeability barrier limited by adjacent melt trajectories. Each swath spans a length L^s of the ridge axis. In the models discussed here L^s is 3 km on average but varies dramatically along the ridge axis, with a maximum of the order of the mesh resolution.

[41] Each swath is divided into a predefined number of quadrilateral tiles (Figure 5b). The temperature profile below the center of each tile is converted into melt fraction according to equation (4). Assuming that all the melt above a critical melt fraction $F_c = 1\%$ migrates upward, the profile of melt production rate p beneath each tile is defined as

$$p = \begin{cases} 0 & \text{if } F < F_c, \\ \max\left(v_z \frac{\partial F}{\partial z}, 0\right) & \text{if } F \geq F_c \end{cases} \quad (9)$$

The melt flux f^t collected by each tile and the average melt fraction F_A^t of the aggregate melt are then given by

$$f^t = \int_{z_b}^{z_k} p \, dz \quad (10)$$

$$F_A^t = \frac{1}{f^t} \int_{z_b}^{z_k} F p \, dz \quad (11)$$

This computation ignores any melt that may be lost by cooling and crystallization as it travels along the permeability barrier [Ghods and Arkani-Hamed, 2000; Cannat et al., 2008].

[42] The crustal thickness, H^s , and average melt fraction, F_a^s , along the section of the ridge axis at the end of each swath are given by

$$H^s = \frac{1}{2V_p L^s} \sum f^t A^t \quad (12)$$

$$F_a^s = \frac{1}{2V_p L^s} \sum F_A^t f^t A^t \quad (13)$$

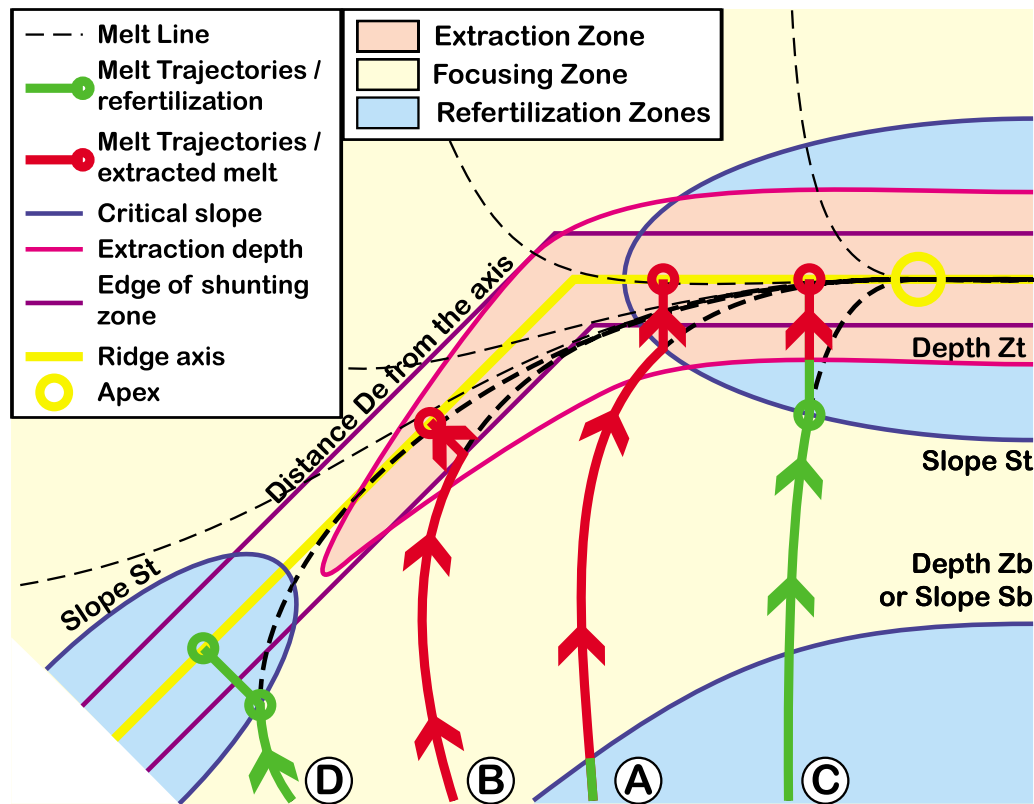


Figure 6. Schematic representation of the extraction, focusing, and refertilization zones in map view for an idealized ridge system. The focusing zone corresponds to the permeability barrier where it is shallower than Z_b and its slope exceeds S_b or S_r . The rest of the barrier forms refertilization zones, except if the barrier is shallower than the extraction depth Z_r . Extraction also occurs in a shunting zone limited by a distance D_e of the plate boundary and shallower than Z_r . Black dashed lines indicate example melt lines, which follow the direction of maximum slope of the permeability barrier to a point where its depth is minimum (apex, yellow circle). Four examples of melt trajectory, color-coded in red or green if the melt collected there is extracted at the ridge axis or refertilizes the mantle, are indicated by the letters A to D and are discussed in the text. Melt is focused along trajectories marked by arrows. Otherwise melt refertilizes the mantle without sub-horizontal migration.

where A^i is the area of each tile and the summation is conducted only on the tiles from which melt is extracted, according to the definitions above. A parallel computation keeps track of the cryptic crust that refertilizes the mantle.

[43] The crust at a given location of the plate boundary is usually contributed by two swaths located on either side of the ridge axis. Imperfect overlap between swaths, which are defined independently from one another, and imprecisions related to the tessellation in the finite element discretization result in short wavelength noise in the raw crustal thickness profile. Therefore, we smooth the profile over a length scale of 10 km, which not only reduces spurious perturbations, but can also be thought to represent crustal level along-axis redistribution of magma in dikes [Fialko, 2001; Gregg et al., 2007]. The length scale of 10 km is sufficient to remove the local perturbations, but does not remove larger-scale anomalies associated with the changes in the geometry of the plate boundary near JMS and Narrowgate.

[44] The entire melt migration algorithm is programmed in Matlab, taking advantage of the scripts `min_dist_between_two_polygons` and `fastsmooth` contributed to MatlabCentral. The only function calls to the finite element model are to

define the permeability barrier surface and extract the vertical column beneath each tile. Thus, this strategy can be fairly easily adapted to other numerical models. The source code is available upon request to the corresponding author.

5.2. Model Results

[45] The crustal thickness profile and the associated variations in the average and maximum degrees of melting of the pooled melt for our preferred model (Configuration A in Table 1 and melt migration parameters in Table 2) are shown in Figure 7. The maximum degree of melting is less than 13%, which is insufficient for clinopyroxene exhaustion. This model successfully predicts increased crustal thickness at JMS and Narrowgate with only minor crustal thickness variations at the longer segments. No crust is extracted at the OS2 oblique supersegment and no cryptic crust is formed anywhere in the model, implying that the melt generated beneath OS2 is extracted elsewhere along the ridge axis.

[46] We explored a range of values for the melt extraction parameters Z_b , S_b , and D_e (Table 2) and document their effect on the resulting crustal thickness profile (Figure 8). In the

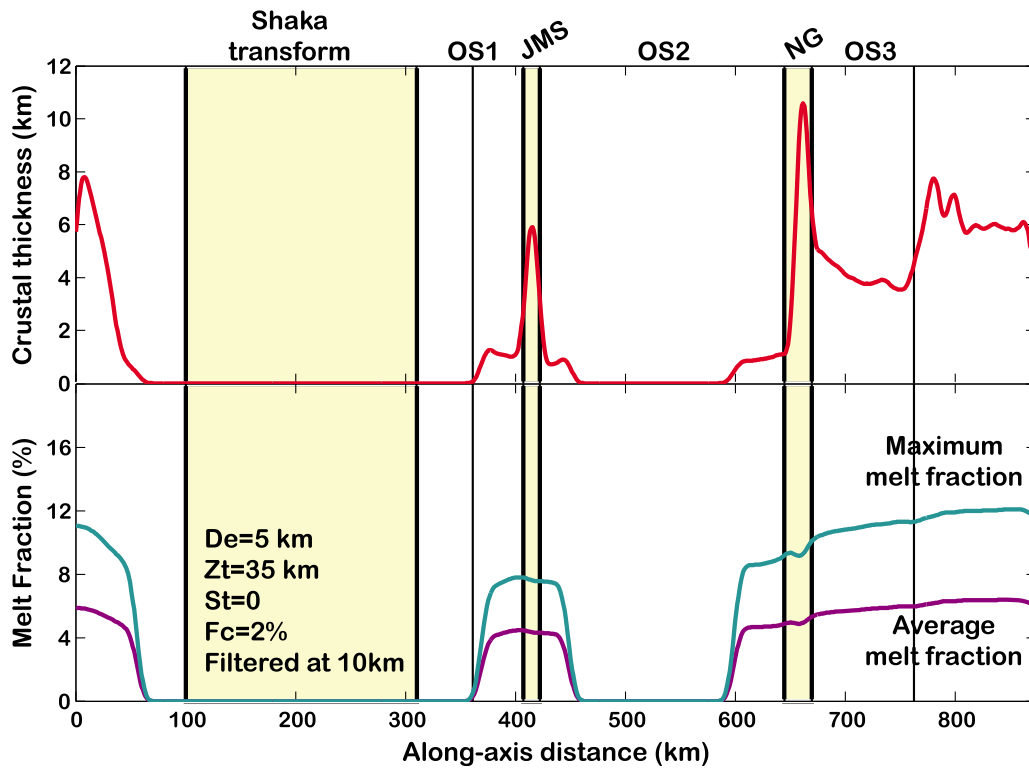


Figure 7. Variations of (top) crustal thickness and (bottom) average and maximum degree of melting against along-axis distance for our preferred model (Configuration A in Table 1) and the melt migration parameters defined in Table 2.

absence of a shunting zone and with $S_t = 0$ (purple curve in Figure 8c), melt thickness is highly heterogeneous, as nothing prevents the individual melt trajectories from reaching the apexes of the permeability barrier. Such models predict a large crustal thickness anomaly at JMS, which coincides with one of the apexes of the permeability barrier. However, at Narrowgate, where no apex is present, there is no crustal thickness anomaly. Furthermore, crustal thickness varies by over a factor of three along the orthogonal supersegment.

[47] Based on these calculations, shunting by the ridge axis is necessary to produce realistic crustal thickness variations. Shunting prevents melts from crossing the ridge axis above a certain depth, which happens otherwise due to the difference between the geometry of the spreading center and that of the permeability barrier. If the shunting distance $D_e = 0$ km, melt is simply prohibited to cross a vertical plane that extends underneath the plate boundary. This produces crustal thickness anomalies at JMS and Narrowgate, but leaves strong fluctuations in crustal thickness are predicted along the less oblique OS3 segment if $S_t = 0$. A shunting zone a few km wide is sufficient to distribute melt continuously along the axis of the orthogonal supersegment even for $S_t = 0$. Localized crustal thickness anomalies are predicted at both JMS and Narrowgate for $D_e < 10$ km.

[48] Increasing the critical slope, S_b , also produces a smoother profile of crustal thickness (Figure 8b). However, values of $S_t > 0.1$ spread the JMS anomaly over 50 km to either side of the seamount, and if $S_t > 0.2$ no crustal thickness anomaly is observed at the Narrowgate segment. Thus, we favor $S_t < 0.1$. Appendix A presents a scaling

analysis of pressure gradients and melt velocity in the decompaction channel that implies that focussing is likely even if S_t is less than 0.01 and *Hebert and Montési* [2010] argue that focusing is limited by slopes of order 0.05 to fit global trends of crustal thickness versus spreading rate.

[49] Finally, we find that the extraction depth, Z_t , must be greater than 30 km for melt to be extracted at JMS (Figure 8a). If this depth is increased further (e.g., $Z_t = 40$ km) melt is extracted along the OS2 supersegment and the amplitude of the crustal thickness anomalies at JMS and Narrowgate is reduced. This confirms that JMS and Narrowgate are composed of melts generated along the OS2 segment but not extracted there because they migrate along the axis to JMS and Narrowgate. Shallow refertilization of the mantle occurs only near JMS and if $Z_t \leq 30$ km.

6. Discussion

6.1. Origin of Crustal Thickness Anomalies at Joseph Mayes Seamount and the Narrowgate Segment

[50] Our most successful melt extraction model (Figure 7) was obtained for an extraction depth of $Z_t = 35$ km, shunting within $D_e = 5$ km of the ridge axis, and a critical focusing slope $S_t = 0$. These results are robust against changes in mantle temperature. Simplifying the mantle rheology to ignore temperature-dependence or yield strength has only a minor effect on the calculated thermal structure. However, these rheological assumptions, especially the incorporation of a yield strength, would likely have stronger effects at higher spreading rate [*Behn et al.*, 2007; *Gregg et al.*, 2009].

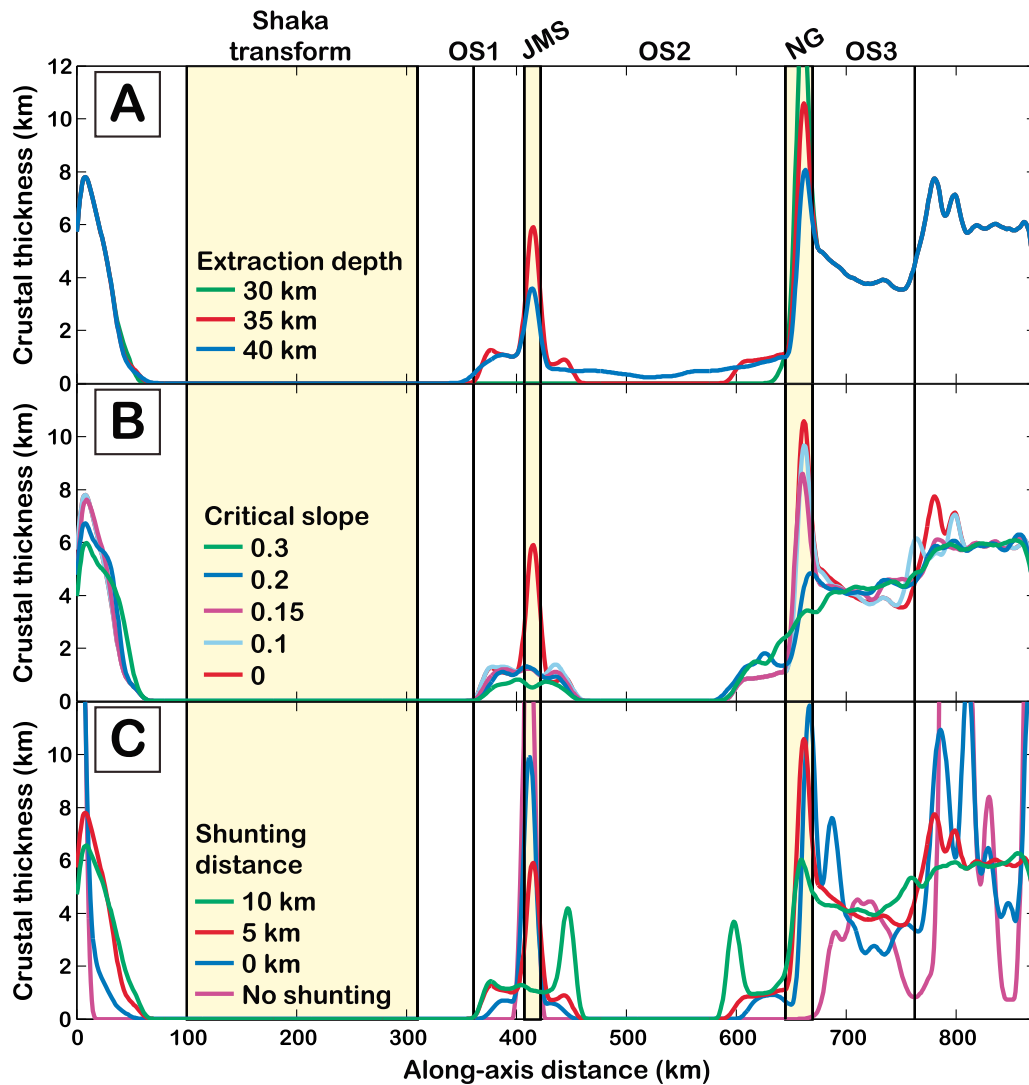


Figure 8. Effect of varying the melt extractions parameters (a) extraction depth, Z_e , (b) critical slope, S_c , and (c) shunting distance, D_e , on the crustal thickness profile. The preferred model (Figure 7) is shown in red in each panel, and the melt extraction parameters are as in the preferred model unless specified.

[51] Beneath JMS, our calculations show an apex in the permeability barrier, which is elongated parallel to the strike of the oblique supersegment (Figure 9a). Melt collects at this apex unless limits on melt propagation defocus melt onto the neighboring oblique segments (e.g., if $S_c > 0^\circ$ melt cannot reach the apex before stagnating). Thus, the melt migration parameters in our preferred model act to enhance the melting anomaly shown in Figure 4 by collecting most of the melt in this region to the JMS segment.

[52] On the other hand, Narrowgate is not associated with an on-axis melting anomaly nor an apex in the permeability barrier. Instead, melts generated on the wings of the OS2 oblique supersegment are deviated toward the Narrowgate segment by the difference in obliquity between the OS2 and the less oblique OS3 segments. Narrowgate's location at the inside corner between these two segments results in the shunting of melt lines from the OS2 segment toward the Narrowgate segment (Figure 9b).

[53] To illustrate this effect, we repeated our study with two simplified ridge geometries (Table 1). Configuration B

ignores the short orthogonal segments at JMS and Narrowgate, but retains the obliquity variations between the longer segments. Crustal thickness anomalies are present at Narrowgate and at the western end of the orthogonal supersegment, although the Narrowgate anomaly has a smaller amplitude than in our preferred model. No anomaly is detected at JMS, suggesting that given the similar obliquities of the OS1 and OS2 segments, orthogonal spreading is necessary to explain this seamount.

[54] Configuration C replaces the entire study area by a straight oblique segment joining the Shaka transform to the orthogonal supersegment. This configuration serves as a control case, as no crustal anomaly is expected at the JMS and Narrowgate segments. Indeed, the crust is uniform along the OS2 supersegment, with a narrow zone of thickened crust at the transition to the orthogonal supersegment (Figure 10). This is consistent with our interpretation that changes in obliquity can focus melts and confirms that in the absence of buoyancy-driven flow, the thickened crust at Narrowgate is caused by its position at the intersection of two segments with different obliquities.

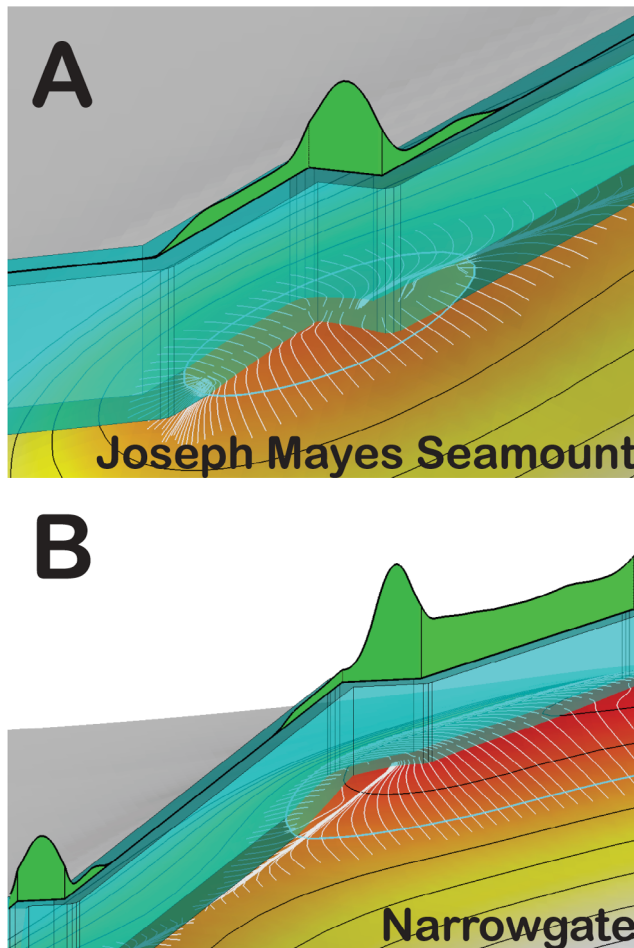


Figure 9. Details of a 3-D visualization of the permeability barrier near the (a) JMS and (b) Narrowgate areas as seen from the Antarctic side of the ridge axis in our preferred model. The barrier is color-coded with depth at 5-km contours. Melt lines are shown in white on the barrier. The cyan contour indicates the maximum depth of melt extraction (35 km) and the blue region marks the shunting zone. The profile of crustal thickness from Figure 7 is reproduced as the green surface above the ridge axis.

[55] The gravity anomalies of the study area (Figure 2) display only minor anomalies that are not captured by our model. For example, a faint bull's-eye of low RMBA at 12°E may be evidence for small buoyancy-driven diapiric instability.

6.2. Melt Extraction in the SWIR 10°–16° Area

[56] Based on the critical effective spreading rate distinguishing slow and ultraslow ridge morphologies, *Montési and Behn* [2007] proposed that melt extraction becomes extremely inefficient when the TBL thickness exceeds 30 km. However, if the maximum depth, Z_t , from which melt can be extracted is ≤ 30 km, no melt would reach the surface at JMS (Figure 8a). On the other hand, if $Z_t = 40$ km, melt is extracted continuously along OS2 and the crust at Narrowgate is less thick than the crust at the orthogonal supersegment. Melt loss due to crystallization during transport to the surface [*Cannat et al.*, 2008] would also reduce the amplitude of the crustal thickness anomalies. Thus, for

the crustal thickness anomalies at JMS and Narrowgate to be explained solely in terms of melt migration and passively driven mantle flow, Z_t is constrained to a narrow window around 35 km. In general, this value is preferred compared to our earlier study *Montési and Behn* [2007], because of the more realistic rheological model used here and the incorporation of 3-D melt migration. However, heat released by the crystallization of melts pooled beneath JMS could thermally erode the lithosphere, resulting in a thinner TBL than predicted by our models [e.g., *Katz*, 2008]. Thermal erosion or any other mechanism that can thin the TBL would imply a shallower allowable extraction depth. Reducing Z_t would also reduce the likelihood of extraction at the oblique supersegment, as TBL erosion would likely be less efficient there, further increasing the amplitude of the crustal thickness anomalies at JMS and Narrowgate.

[57] Shunting simulates the effect of ridge-axis structures, such as faults or dikes, on melt extraction. Conceptually, the shunting zone is similar to the zone of crust accretion, which many studies have documented to be of the order of 1 or 2 km [e.g., *Macdonald*, 1982; *Sinton and Detrick*, 1992]. While we cannot confidently resolve whether $D_e = 5$ km is required to explain crustal thickness variations in the study area or if smaller values would be acceptable, a robust conclusion of our models is that shunting is required. *Standish and Sims* [2010] documented a 10-km wide accretion zone at Narrowgate, which they argued was a consequence of melt extraction along faults rooted in a narrow zone at 20 km depth. Our models imply that ridge axis structures influence melt extraction at up to 30 km depth near the ridge axis. These predictions can be reconciled if cracking takes place within the shunting zone. Inclined faults rooted beneath the axis could widen the extraction zone to ≥ 10 km (Figure 11).

[58] Our models indicate that the anomalous crustal thicknesses of JMS and Narrowgate are due to an increased contribution of low-degree melts generated at the wings of the oblique supersegment melting area. However, the average degree of melting of the pooled melts in these areas is calculated to decrease by only 1 or 2% (Figure 7). Larger variations are predicted between the major segments of the study area. This implies that the chemical variations documented by *Standish et al.* [2008] do not result solely from melt focusing, but as they proposed, require a contribution from an enriched, mafic lithology. The success of our melt migration model at reproducing crustal thickness variations supports the hypothesis that this enriched lithology is widespread in the study area, and is not indicative of a small-scale plume. Trace elements data from basalts [*Le Roex et al.*, 1992; *Standish*, 2005] and abyssal peridotites [*Warren et al.*, 2009] indicate that melts from the Bouvet hot spot have likely metasomatized the region prior to melting related to the current spreading center. Our model is consistent with the proposition that Bouvet metasomatism is at least partially responsible for the chemical variations of basalts at JMS and Narrowgate.

6.3. Role of Serpentinization

[59] Gravity anomalies at the OS2 oblique supersegment do not indicate significant crustal thinning relative to the reference model (Figure 2), although our crustal thickness calculations imply near-zero crustal thickness consistent with the composition of dredge hauls and the absence of

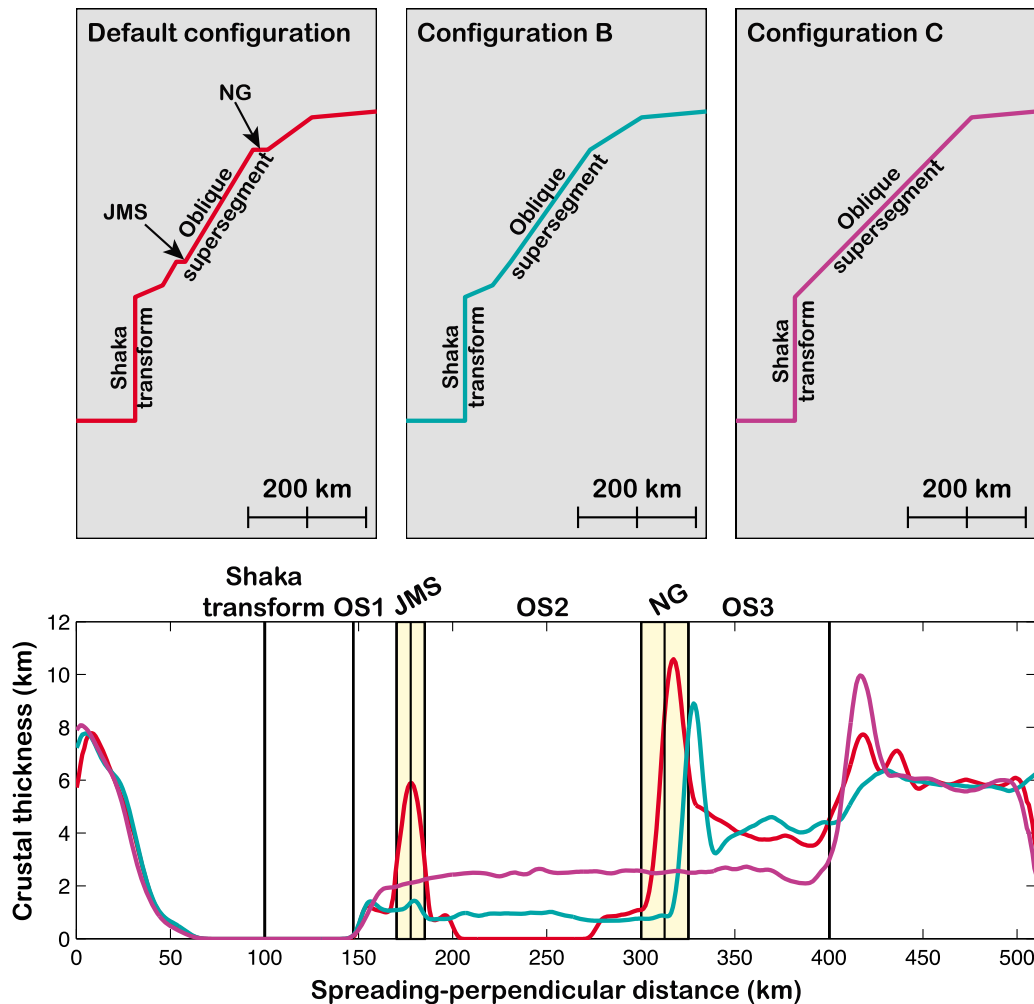


Figure 10. Importance of the ridge geometry on crustal thickness variations. The preferred model (Figure 7) is shown in red. Configuration B (teal) ignores the short orthogonal segments at JMS and Narrowgate, while Configuration C (purple) features a single straight oblique segment. See Table 1 for segment definitions. Note that the x-coordinate is different from previous profiles.

magnetic anomalies at OS2 [Dick *et al.*, 2003]. These apparently contradictory observations can be reconciled if significant serpentinization of the mantle occurs beneath the OS2 supersegment. The density of serpentinized peridotite is similar to that of gabbroic crust, making it impossible to differentiate between these lithologies from gravity alone. However, because serpentine is stable only at low temperatures, we can use our thermal model to evaluate the possible importance of serpentine across the study area. We first determine the region of serpentine stability by computing the depth of the 450°C isotherm beneath the axis. A portion R of the mantle above that isotherm is then assumed to be transformed into serpentine, and we report the equivalent thickness of low density material (Figure 12).

[60] Serpentinization has the strongest effect on the OS1 and OS2 segments because the lithosphere is coldest in these regions. By contrast, serpentinization only slightly affects JMS and the OS3 segments and has no effect on the warmer orthogonal supersegment or the Narrowgate area. Overall, we find that a serpentinization fraction of $R \approx 0.6$ above the 450°C isotherm produces similar thicknesses of low-density

material beneath all the major segments in the study area, while preserving the crustal thickness anomalies of JMS and Narrowgate.

[61] Using a more sophisticated thermodynamic model, Iyer *et al.* [2010] showed that a thick serpentinized layer forms on-axis only at the slowest spreading ridges, corroborating our suggestion that serpentinization is only important at the OS1 and OS2 segments. Abyssal peridotites from our study area have been intensely serpentinized [Dick *et al.*, 2003; Warren *et al.*, 2009] but no correlation between degree of serpentinization and segment obliquity has been reported. Additional geophysical data will be necessary to constrain if serpentinization is more intense or reaches greater depth at the most oblique segments.

6.4. Segmentation at Ultraslow Ridges

[62] One major difference between ultraslow and faster spreading ridges is the character of segmentation. While ultraslow ridges do not have transform offsets, they display variations in obliquity that are sometimes described as non-transform offsets [Mendel *et al.*, 1997; Rommevaux-Jestin

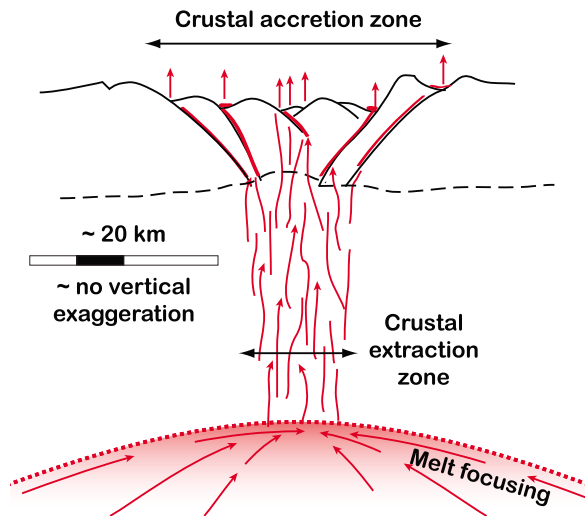


Figure 11. Schematic representation of the melt extraction network at an ultraslow magmatic center like Narrowgate. Melt is focused at depth along a permeability barrier (red dotted line with shading representing melt content) until it enters a ~ 10 km wide and ~ 35 km deep extraction region in which melt is dominantly extracted along dikes (red lines). Near the surface, melt is redistributed along faults (black lines, lined with red where melt is present) within a 20 km wide crust accretion zone, as proposed by *Standish and Sims* [2010]. The dashed line represents the base of the anomalously thick crust at the magmatic centers and arrows represent melt migration trajectories.

et al., 1997]. Our model links crustal thickness variations with changes in obliquity, whereas *Cannat et al.* [2006] argued that variations in melt supply control obliquity. In an earlier study of the eastern end of the SWIR, from 62°E to 66°E, *Cannat et al.* [2003] showed that areas of orthogonal spreading follow localized increases in crustal thickness. They proposed that melt collects along axis to form magmatically robust regions where melt is extracted via dikes and these dikes are oriented perpendicular to the spreading

direction and generate orthogonal segments [*Cannat et al.*, 2006, 2008].

[63] This dike-intrusion control on obliquity is a plausible explanation for the formation of the Narrowgate segment. We show that the melting anomaly at Narrowgate does not require the presence of an area of orthogonal spreading; the difference in obliquity between the OS2 and OS3 segments can produce a crustal thickness anomaly at the location of Narrowgate (Figure 10). Diking in the focus zone between the OS2 and OS3 segments of our model B, which does not feature orthogonal spreading, may have reoriented this portion of the ridge to become orthogonal to the spreading direction, giving birth to the Narrowgate segment. Once established, this oblique-orthogonal-oblique geometry will increase melt focusing and crustal thickness at Narrowgate (Figure 10). However, diking is not the sole contributor to melt extraction at Narrowgate. For example, faulting is necessary to explain the bathymetric relief and the width of the melt extraction zone [*Standish and Sims*, 2010]. Moreover, both preexisting faults [*Behn et al.*, 2002; *Deschamps et al.*, 2005] and lithosphere thickness variations can reorient stress directions. Thus, a lithospheric-scale stress interaction model is necessary to evaluate the likely orientation of dikes at the Narrowgate area.

[64] It is more difficult to explain JMS as the sole result of dike intrusions because the obliquity contrast between the OS1 and OS2 segments in our model B is not sufficient to focus melt (Figure 10). JMS may reflect a diapiric instability in the mantle or an instability in the permeability barrier generated by a feedback between latent heat release and barrier depth [*England and Katz*, 2010]. Similar instabilities may explain the small magmatic zone at 12.5°E. In such a scenario, dike-related obliquity variations would have enhanced the instability at JMS but not at 12.5°E, possibly because the obliquity is higher at 12.5°E, requiring a stronger reorientation of the axis to become orthogonal.

[65] The origin of the large-scale segmentation that defines the oblique OS1, OS2, and OS3 segments is unclear at present. It appears to have been stable over long timescales [*Dick et al.*, 2003; *Sauter et al.*, 2004], in contrast to the many short-lived segments observed at 61°–66°E along the SWIR

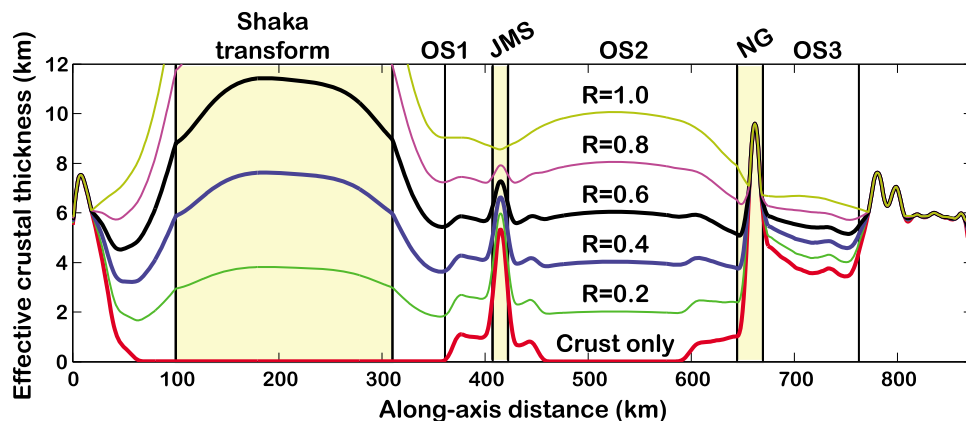


Figure 12. Effect of serpentinization on effective crustal thickness, defined as the total amount of low density material underneath the axis. The parameter R indicates the fraction of the mantle colder than 450°C that is transformed into serpentine.

[Cannat *et al.*, 2006]. The geometry of continental rupture is thought to affect the observed obliquity variation of the current Gakkel ridge axis [Michael *et al.*, 2003]. However, the SWIR area was likely affected by the passage of the Bouvet hot spot [Standish *et al.*, 2008; Warren *et al.*, 2009], possibly wiping out any earlier segmentation patterns. Cannat *et al.* [2008] inferred that the mantle below the orthogonal supersegment may be 20° cooler and/or less fertile than the mantle below the oblique supersegment, which could reflect a waning influence of the Bouvet hot spot. Moreover, the remarkable coincidence of the Shaka transform and the Bouvet hot spot track also suggests that the passage of the hot spot may have significantly affected the geometry of the ridge.

7. Conclusion

[66] The ultraslow-spreading 10°–16°E area of the SWIR features crustal thickness variations that can be understood in the context of plate-driven mantle flow and 3-D melt focusing along a permeability barrier at the base of the lithosphere. To reproduce the geologically inferred crustal thickness variations, our modeling indicates that: (1) JMS is located atop a local minimum in lithosphere thickness that collects melts produced nearby; (2) the Narrowgate area taps melts that are focused due to the different obliquities of the adjacent ridge segments; and (3) non-crustal low-density material, probably partially serpentinized mantle, is necessary to explain RMBA along the OS2 segment.

[67] These three conclusions from our melt migration modeling are compatible with each other. Specifically, if melt is extracted from depths of 35 km within a 10-km wide zone centered around the ridge axis, and 60% of the mantle colder than 450°C is serpentinized, the geological and geophysical constraints on melting and crustal accretion in the study area can all be satisfied. However, other processes, such as buoyancy-driven instabilities and/or thermal and chemical interaction between the lithosphere and ascending magma, are likely to influence melt extraction. Future studies should evaluate these processes and determine how they may influence the patterns of melting and melt migration in this and other, faster-spreading ridge environments.

Appendix A: Scaling Relations and Validity of Model Assumptions

[68] The success of our approach to capture variations of crustal thickness at the SWIR 10°–16° area implies that the assumptions underlying our model are reasonable and may be applicable to other ridges.

[69] We assume vertical melt trajectories underneath the permeability barrier. To determine if such trajectories are realistic, it is useful to refer to a corner flow solution for mantle flow perpendicular to the ridge axis

$$v_x^c = V_e \frac{2}{\pi} (\theta - \sin \theta \cos \theta) \quad (\text{A1})$$

$$v_y^c = V_e \frac{2}{\pi} \cos^2 \theta \quad (\text{A2})$$

$$p^c = -\eta V_e \frac{4}{\pi r} \cos \theta \quad (\text{A3})$$

where v_x^c and v_y^c the two components of the velocity field, p^c the associated pressure field, r is the distance from the ridge axis, θ the angle from the vertical direction, and η is the mantle viscosity [McKenzie, 1969; Montési and Behn, 2007].

[70] If the corner flow solution is an acceptable approximation for the flow field across the spreading center, the thickness of the thermal boundary beneath the axis is given approximately by

$$z_{TBL} \approx 5\kappa/V_e \quad (\text{A4})$$

where κ is the thermal diffusivity [Montési and Behn, 2007].

[71] First, we can evaluate the error in the mantle flow field made by neglecting buoyancy. Pressure gradients according to equation (A3) are of order $4\eta V_e/(\pi r^2)$. Buoyancy due to melt produces pressure gradients of order $\phi \Delta \rho g$, where ϕ is the melt porosity, of order of 1% or less [Toomey *et al.*, 1998], $\Delta \rho \sim 300 \text{ kg/m}^3$ is the density contrast between solid mantle and melt, and g is the acceleration of gravity. Substituting z_{TBL} from equation (A4) for r , we see that buoyancy has a smaller effect than corner flow if

$$V_e > \left(\frac{25\pi\kappa^2\phi\Delta\rho g}{4\eta} \right)^{1/3} \quad (\text{A5})$$

[72] If $\kappa = 10^{-6} \text{ m}^2$ and $\eta_0 = 10^{19} \text{ Pa s}$, buoyancy can be ignored if $V_e > 1 \text{ cm/yr}$. Our study area is slower than this, which would indicate that buoyancy should be taken into account. However, as we are able to match the pattern observed in the study area, buoyancy may be less important than implied by this scaling analysis. It is possible that the relevant buoyancy gradients are less than used here because buoyancy manifests itself as a convective mode [Rabinowicz *et al.*, 1984; Su and Buck, 1993; Katz, 2010] with a length scale that is different from z_{TBL} . Also, melt migration follows the shape of the thermal boundary layer near the surface, which may be less affected by mantle buoyancy than the warmer asthenosphere. Nevertheless, future studies, should seek to explain the same signals without neglecting buoyancy.

[73] We next evaluate the relative importance of pressure gradients that arise from the mantle flow field and magma buoyancy on melt migration [Phipps Morgan, 1987; Spiegelman and McKenzie, 1987]. The melt velocity \mathbf{v}^f is given by

$$\mathbf{v}^f = \mathbf{v}^c + \frac{k}{\phi\eta_f} (-\Delta\rho g \hat{\mathbf{e}}_z + \nabla p^c) \quad (\text{A6})$$

where k is the permeability, $\eta_f \approx 10 \text{ Pa s}$ is the melt viscosity [Ryan and Blevins, 1987] and $\hat{\mathbf{e}}_z$ a unit vector in the vertical direction [e.g., Sleep, 1974; McKenzie, 1984; Scott and Stevenson, 1984].

[74] Melt buoyancy induces a pressure gradient of the order of $\Delta\rho g \approx 3 \text{ MPa/km}$. Therefore, pressure gradients due to mantle flow (equation (A3)) dominate over buoyancy only if its viscosity exceeds

$$\eta_c = \frac{25\pi\Delta\rho g\kappa^2}{4V_e^3} \quad (\text{A7})$$

This critical viscosity increases rapidly as spreading rate decreases. At the transition to ultraslow spreading, 6 mm/yr,

it reaches 7×10^{21} Pa s, almost 1000 times greater than estimates for asthenospheric viscosity beneath ridges [e.g., *Hirth and Kohlstedt*, 2003]. For $\eta_0 = 10^{19}$ Pa s, pressure gradients driven by mantle flow are comparable to those due to buoyancy only if the effective spreading rate exceeds ≈ 24 cm/yr half rate, three times faster than the fastest ridges on Earth. Furthermore, equation (A3) implies that even for the fastest spreading rate currently observed (~ 7.5 cm/yr) pressure gradients induced by mantle flow only dominate at depths < 1.5 km, a length scale so small that the corner flow solution and this scaling analysis are not applicable. Therefore, it is likely that buoyancy is the dominant source of pressure gradients for melt migration at every spreading rate.

[75] The permeability of the mantle to melt migration depends on porosity according to

$$k = k_0(\phi/\phi_0)^n \quad (\text{A8})$$

where $k_0 = 10^{-11} \text{ m}^2$ for a grain size of 1 cm [*Behn et al.*, 2009] and $\phi_0 = 0.02$, and $n = 2$ or 3 for idealized and heterogeneous networks, respectively [*von Bagen and Waff*, 1986; *Zhu and Hirth*, 2003]. *Zhu et al.* [2011] show that a highly connected melt network is present in a partially molten aggregate even at the low porosities inferred beneath mid-ocean ridges. Thus, from equation (A6), buoyancy induces a melt velocity of 1 m/yr at a residual 1% porosity, independent of spreading rate. Equations (A1) and (A2) imply a mantle flow velocity everywhere comparable to V_e , of order of 0.1 m/yr, and therefore always much smaller than the vertical melt velocity. Furthermore, thorium disequilibrium in mid-ocean ridge glasses implies even faster magma ascent rates, in excess of 10 m/yr [*Gill and Condomines*, 1992; *Sims et al.*, 2002; *Lundstrom et al.*, 1995]. Rapid melt transport can take place in dissolution channels [*Iwamori*, 1994; *Kelemen and Dick*, 1995; *Aharonov et al.*, 1995; *Spiegelman et al.*, 2001; *Jull et al.*, 2002] where the increased porosity and reduced pyroxene content would increase permeability [*Zhu and Hirth*, 2003].

[76] In summary, fast melt velocities and the dominance of melt buoyancy imply that mantle flow can indeed be safely ignored at slow and ultraslow ridges and probably at all spreading rate when considering melt migration. Thus, the assumption of vertical melt trajectories is likely valid until very close to the TBL and the permeability barrier.

[77] Our model also implies that melts can propagate along the barrier even if its slope, S , is less than less 0.1. Melt migration is driven by pressure gradients along the barrier. In a thin, open channel, these pressure gradients are approximately equal $S\Delta\rho g$ and induce a melt velocity of

$$v_x^f \approx \frac{kS\Delta\rho g}{\phi\eta_f} - v_x^c \quad (\text{A9})$$

Thus, equation (A8) implies that focusing is possible if

$$S\left(\frac{\phi}{\phi_0}\right)^{n-1} \geq \frac{V_e \eta_f \phi_0}{k_0 \Delta\rho g} \quad (\text{A10})$$

in the decompaction zone immediately below the permeability barrier. A critical slope of 0.1 and $\eta_f = 10$ Pa s [*Ryan and Blevins*, 1987] would enable focusing even at the fastest spreading ridges (150 mm/yr) even if porosity were only

0.6% with $n = 2$ or 1.1% if $n = 3$. Porosity might reach 20% in the decompaction channel, although magma flow along the barrier may reduce this number significantly [*Sparks and Parmentier*, 1991]. 20% porosity enables focusing at slopes of 0.003 at ultrafast spreading or 1.7×10^{-4} at the slow-ultraslow transition if $n = 2$, ten times smaller if $n = 3$. *Hebert and Montési* [2010] constrained a minimum focusing slope of 0.05, implying that if the porosity in the decompaction channel porosity is larger than 0.3%, focusing will occur at all spreading rates.

[78] **Acknowledgments.** This work was supported by grants OCE-0623188 and OCE-0937277 from the National Science Foundation. We thank Tom O'Haver and Guillaume Jacquenot for contributing their routines `fastsmooth`, and `min_dist` between two polygons to `MatlabCentral` (<http://www.mathworks.com/matlabcentral>), and Henry Dick, Jeff Standish, and Jessica Warren for insightful discussions on the geology and geochemistry of this region. Richard F. Katz, David W. Sparks, and Associate Editor Michael P. Ryan provided insightful and constructive reviews. COMSOL Multiphysics® is a registered trademark of COMSOL AB. All spreading rates were obtained using Bill Menke's online plate velocity calculator (<http://www.ldeo.columbia.edu/users/menke/plates2.htm>). J.L. Barry participated to this project as a WHOI summer student fellow.

References

- Aharonov, E., J. A. Whitehead, P. B. Kelemen, and M. Spiegelman (1995), Channeling instability of upwelling melt in the mantle, *J. Geophys. Res.*, *100*, 20,433–20,450, doi:10.1029/95JB01307.
- Asimow, P. D., and C. H. Langmuir (2003), The importance of water to oceanic mantle melting regimes, *Nature*, *421*, 815–820, doi:10.1038/nature01429.
- Behn, M. D., J. Lin, and M. T. Zuber (2002), Evidence for weak oceanic transform faults, *Geophys. Res. Lett.*, *29*(24), 2207, doi:10.1029/2002GL015612.
- Behn, M. D., M. S. Boettcher, and G. Hirth (2007), Thermal structure of oceanic transform faults, *Geology*, *35*(4), 307–310, doi:10.1130/G23112A.1.
- Behn, M. D., G. Hirth, and J. R. Elsenbeck II (2009), Implications of grain size evolution on the seismic structure of the oceanic upper mantle, *Earth Planet. Sci. Lett.*, *282*(1–4), 178–189, doi:10.1016/j.epsl.2009.03.014.
- Bercovici, D. (2003), The generation of plate tectonics from mantle convection, *Earth Planet. Sci. Lett.*, *205*(3–4), 107–121, doi:10.1016/0012-821X(96)00140-9.
- Bown, J. W., and R. S. White (1994), Variation with spreading rate of oceanic crustal thickness and geochemistry, *Earth Planet. Sci. Lett.*, *121*(3–4), 435–449, doi:10.1016/0012-821X(94)90082-5.
- Brunelli, D., M. Seyler, A. Cipriani, L. Ottolini, and E. Bonatti (2006), Discontinuous melt extraction and weak refertilization of mantle peridotites at the Vema lithospheric section (Mid-Atlantic Ridge), *J. Petrol.*, *47*(4), 745–771, doi:10.1093/petrology/egi092.
- Canales, J. P., M. R. Nedimović, G. M. Kent, S. M. Carbotte, and R. S. Detrick (2009), Seismic reflection images of a near-axis melt sill within the lower crust at the Juan de Fuca ridge, *Nature*, *460*, 89–93, doi:10.1038/nature08095.
- Cannat, M. (1996), How thick is the magmatic crust at slow spreading oceanic ridges?, *J. Geophys. Res.*, *101*, 2847–2857, doi:10.1029/95JB03116.
- Cannat, M., C. Rommevaux-Jestin, and H. Fujimoto (2003), Melt supply variations to a magma-poor ultra-slow spreading ridge (Southwest Indian Ridge 61° to 69°E), *Geochem. Geophys. Geosyst.*, *4*(8), 9104, doi:10.1029/2002GC000480.
- Cannat, M., D. Sauter, V. Mendel, E. Ruellan, K. Okino, J. Escartin, V. Combier, and M. Baala (2006), Modes of seafloor generation at a melt-poor ultraslow-spreading ridge, *Geology*, *34*(7), 605–608, doi:10.1130/G22486.1.
- Cannat, M., D. Sauter, C. Meyzen, E. Humler, and M. Le Rigoleur (2008), Spreading rate, spreading obliquity, and melt supply at the ultraslow spreading Southwest Indian Ridge, *Geochem. Geophys. Geosyst.*, *9*, Q04002, doi:10.1029/2007GC001676.
- Chen, Y., and W. J. Morgan (1990), A nonlinear rheology model for mid-ocean ridge axis topography, *J. Geophys. Res.*, *95*, 17,583–17,604, doi:10.1029/JB095iB11p17583.
- DeMets, C., R. G. Gordon, D. F. Argus, and S. Stein (1994), Effect of recent revisions to the geomagnetic reversal time scale on estimates of current plate motions, *Geophys. Res. Lett.*, *21*(5), 2191–2194, doi:10.1029/94GL02118.

- Deschamps, A., T. Fujiwara, M. Asada, L. Montési, and P. Gente (2005), Faulting and volcanism in the axial valley of the slow-spreading center of the Mariana back arc basin from Wadatumi side-scan sonar images, *Geochem. Geophys. Geosyst.*, *6*, Q05006, doi:10.1029/2004GC000881.
- Dick, H. J. B., J. Lin, and H. Schouten (2003), An ultraslow-spreading class of ocean ridge, *Nature*, *426*, 405–412, doi:10.1038/nature02128.
- Dick, H. J. B., C. J. Lissenberg, and J. M. Warren (2010), Mantle melting, melt transport, and delivery beneath a slow-spreading ridge: The paleo-MAR from 23° 15'N to 23° 45'N, *J. Petrol.*, *51*(1–2), 425–467, doi:10.1093/petrology/egp088.
- England, P. C., and R. F. Katz (2010), Melting above the anhydrous solidus controls the location of volcanic arcs, *Nature*, *467*, 700–703, doi:10.1038/nature09417.
- Fialko, Y. (2001), On origin of near-axis volcanism and faulting at fast spreading mid-ocean ridges, *Earth Planet. Sci. Lett.*, *190*(1–2), 31–39, doi:10.1016/S0012-821X(01)00376-4.
- Fornari, D. G., D. G. Gallo, M. H. Edwards, J. A. Madsen, and M. R. Perfit (1989), Structure and topography of the siqueiros transform structure and topography of the Siqueiros transform fault system: Evidence of intra-transform spreading centers, *Mar. Geophys. Res.*, *11*(4), 263–299, doi:10.1007/BF00282579.
- Garmany, J. (1989), Accumulations of melt at the base of young oceanic crust, *Nature*, *340*, 628–632, doi:10.1038/340628a0.
- Ghods, A., and J. Arkani-Hamed (2000), Melt migration beneath mid-ocean ridges, *Geophys. J. Int.*, *140*(3), 687–697, doi:10.1046/j.1365-246X.2000.00032.x.
- Gill, J. B., and M. Condomines (1992), Short-lived radioactivity and magma genesis, *Science*, *257*, 1368–1376, doi:10.1126/science.257.5075.1368.
- Gregg, P. C., J. Lin, M. D. Behn, and L. G. J. Montési (2007), Spreading rate dependence of gravity anomalies along oceanic transform faults, *Nature*, *448*, 183–187, doi:10.1038/nature05962.
- Gregg, P. M., M. D. Behn, J. Lin, and T. L. Grove (2009), Melt generation, crystallization, and extraction beneath segmented oceanic transform faults, *J. Geophys. Res.*, *114*, B11102, doi:10.1029/2008JB006100.
- Grindlay, N. R., J. Madsen, C. Rommevaux-Jestin, and J. Sclater (1998), A different pattern of ridge segmentation and mantle Bouguer anomalies along the ultra-slow spreading Southwest Indian Ridge (15° 30'E to 25°E), *Earth Planet. Sci. Lett.*, *161*(1–4), 243–253, doi:10.1016/S0012-821X(98)00154-X.
- Hebert, L. B., and L. G. J. Montési (2010), Generation of permeability barriers during melt extraction at mid-ocean ridges, *Geochem. Geophys. Geosyst.*, *11*, Q12008, doi:10.1029/2010GC003270.
- Hebert, L. B., and L. G. J. Montési (2011), Melt extraction pathways at segmented oceanic ridges: Application to the East Pacific Rise at the Siqueiros transform, *Geophys. Res. Lett.*, *38*, L11306, doi:10.1029/2011GL047206.
- Hékinian, R., D. Bideau, M. Cannat, J. Francheteau, and R. Hébert (1992), Volcanic activity and crust-mantle exposure in the ultrafast volcanic activity and crust-mantle exposure in the ultrafast Garrett transform fault near 13° 28'S in the Pacific, *Earth Planet. Sci. Lett.*, *108*(4), 259–275, doi:10.1016/0012-821X(92)90027-S.
- Hirschmann, M. M. (2000), Mantle solidus: Experimental constraints and the effects of peridotite composition, *Geochem. Geophys. Geosyst.*, *1*(10), 1042, doi:10.1029/2000GC000070.
- Hirth, G., and D. L. Kohlstedt (2003), Rheology of the upper mantle and the mantle wedge: A view from the experimentalists, in *The Subduction Factory*, *Geophys. Monogr. Ser.*, vol. 138, edited by J. Eiler, pp. 83–105, AGU, Washington, D. C.
- Hirth, G., J. Escartin, and J. Lin (1998), The rheology of the lower oceanic crust: Implications for lithospheric deformation at mid-ocean ridges, in *Faulting and Magmatism at Mid-Ocean Ridges*, *Geophys. Monogr. Ser.*, vol. 106, edited by W. R. Buck, P. T. Delaney, J. A. Karson, and Y. Y. Lagabriele, pp. 291–304, AGU, Washington, D. C.
- Isacks, B. L., J. E. Oliver, and L. R. Sykes (1968), Seismology and the new global tectonics, *J. Geophys. Res.*, *73*, 5855–5899, doi:10.1029/JB073i018p05855.
- Iwamori, H. (1994), ^{238}U - ^{230}Th - ^{226}Ra and ^{235}U - ^{231}Pa disequilibria produced by mantle melting with porous and channel flows, *Earth Planet. Sci. Lett.*, *125*(1–4), 1–16, doi:10.1016/0012-821X(94)90203-8.
- Iyer, K., L. H. Rüpke, and J. Phipps Morgan (2010), Exploring the feedbacks between mantle hydration and hydrothermal convection at ocean spreading centers: New insights from numerical modeling, *Earth Planet. Sci. Lett.*, *296*(1–2), 34–44, doi:10.1016/j.epsl.2010.04.037.
- Jull, M., P. B. Kelemen, and K. Sims (2002), Consequences of diffuse and channelled porous melt migration on Uranium series disequilibria, *Geochim. Cosmochim. Acta*, *66*(23), 4133–4148, doi:10.1016/S0016-7037(02)00984-5.
- Kaczmarek, M.-A., and O. Müntener (2008), Juxtaposition of melt impregnation and high-temperature shear zones in the upper mantle: Field and petrological constraints from the Lanzo peridotite (northern Italy), *J. Petrol.*, *49*(12), 2187–2220, doi:10.1093/petrology/egn065.
- Katz, R. F. (2008), Magma dynamics with the enthalpy method: Benchmark solutions and magmatic focusing at mid-ocean ridges, *J. Petrol.*, *49*(12), 2099–2121, doi:10.1093/petrology/egn058.
- Katz, R. F. (2010), Porosity-driven convection and asymmetry beneath mid-ocean ridges, *Geochem. Geophys. Geosyst.*, *11*, Q0AC07, doi:10.1029/2010GC003282.
- Katz, R. F., M. Spiegelman, and C. H. Langmuir (2003), A new parameterization of hydrous mantle melting, *Geochem. Geophys. Geosyst.*, *4*(9), 1073, doi:10.1029/2002GC000433.
- Kelemen, P. B., and E. Aharonov (1998), Periodic formation of magma fractures and generation of layered gabbros in the lower crust beneath oceanic spreading ridges, in *Faulting and Magmatism at Mid-Ocean Ridges*, *Geophys. Monogr. Ser.*, vol. 106, edited by W. R. Buck, P. T. Delaney, J. A. Karson, and Y. Y. Lagabriele, pp. 267–290, AGU, Washington, D. C.
- Kelemen, P. B., and H. J. B. Dick (1995), Focused melt flow and localized deformation in the upper mantle: Juxtaposition of replacive dunite and ductile shear zones in the Josephine peridotite, SW Oregon, *J. Geophys. Res.*, *100*, 423–438, doi:10.1029/94JB02063.
- Kinzel, R. J., and T. L. Grove (1992), Primary magmas of mid-ocean ridge basalts: 1. Experiments and methods, *J. Geophys. Res.*, *97*, 6885–6906, doi:10.1029/91JB02840.
- Korenaga, J., and P. B. Kelemen (1997), Origin of gabbro sills in the Moho transition zone of the Oman ophiolite: Implications for magma transport in the oceanic lower crust, *J. Geophys. Res.*, *102*, 27,729–27,749, doi:10.1029/97JB02604.
- Kuo, B., and D. W. Forsyth (1988), Gravity anomalies of the ridge-transform system in the South Atlantic between 31° and 34.5°S: Upwelling centers and variation in crustal thickness, *Mar. Geophys. Res.*, *10*(3–4), 205–232, doi:10.1007/BF00310065.
- Le Roex, A. P., H. J. B. Dick, and R. T. Watkins (1992), Petrogenesis of anomalous K-enriched MORB from the Southwest Indian Ridge: 11° 53'E to 14° 38'E, *Contrib. Mineral. Petrol.*, *110*(2–3), 253–268, doi:10.1007/BF00310742.
- Le Roux, V., J.-L. Bodinier, A. Tommasi, O. Alard, J.-M. Dautria, A. Vauchez, and A. J. V. Richez (2007), The Lherz spinel lherzolite: Refertilized rather than pristine mantle, *Earth Planet. Sci. Lett.*, *259*(3–4), 599–612, doi:10.1016/j.epsl.2007.05.026.
- Lin, J., and J. Phipps Morgan (1992), The spreading rate dependence of three-dimensional mid-ocean ridge gravity structure, *Geophys. Res. Lett.*, *19*(1), 13–16, doi:10.1029/91GL03041.
- Lundstrom, C. C., J. Gill, Q. Williams, and M. R. Perfit (1995), Mantle melting and basalt extraction by equilibrium porous flow, *Science*, *270*, 1958–1961, doi:10.1126/science.270.5244.1958.
- Macdonald, K. C. (1982), Mid-ocean ridges: Fine scale tectonic, volcanic and hydrothermal processes within the plate boundary zone, *Annu. Rev. Earth Planet. Sci.*, *10*, 155–190, doi:10.1146/annurev.ea.10.050182.001103.
- Macdonald, K. C., P. J. Fox, R. T. Alexander, R. Pockalny, and P. Gente (1996), Volcanic growth fault and the origin of Pacific abyssal hills, *Nature*, *380*, 125–129, doi:10.1038/380125a0.
- Magde, L. S., and D. W. Sparks (1997), Three-dimensional mantle upwelling, melt generation, and melt migration beneath segment slow spreading ridges, *J. Geophys. Res.*, *102*, 20,571–20,583, doi:10.1029/97JB00996.
- Magde, L. S., D. W. Sparks, and R. S. Detrick (1997), The relation between buoyant mantle flow, melt migration, and gravity bull's eyes at the Mid-Atlantic Ridge between 33°N and 35°N, *Earth Planet. Sci. Lett.*, *148*(1–2), 59–67, doi:10.1016/S0012-821X(97)00039-3.
- Mammerickx, J., and D. Sandwell (1986), Rifting of old oceanic lithosphere, *J. Geophys. Res.*, *91*, 1975–1988, doi:10.1029/JB091iB02p01975.
- McKenzie, D. (1984), The generation and compaction of partially molten rock, *J. Petrol.*, *25*(3), 713–765, doi:10.1093/petrology/25.3.713.
- McKenzie, D. P. (1969), Speculations on the consequences and causes of plate motions, *Geophys. J. R. Astron. Soc.*, *18*(1), 1–32, doi:10.1016/S0012-821X(97)00039-3.
- Mendel, V., D. Sauter, L. Parson, and J.-R. Vanney (1997), Segmentation and morphotectonic variation along a super slow-spreading center: The Southwest Indian Ridge (57°E–70°E), *Mar. Geophys. Res.*, *19*(6), 505–533, doi:10.1023/A:1004232506333.
- Michael, P. J., et al. (2003), Magmatic and amagmatic seafloor generation at the ultraslow-spreading Gakkel Ridge, Arctic Ocean, *Nature*, *423*, 956–961, doi:10.1038/nature01704.
- Mitchell, G. A., L. G. J. Montési, W. Zhu, D. K. Smith, and H. Schouten (2011), Transient rifting north of the Galápagos Triple Junction, *Earth Planet. Sci. Lett.*, *307*(3–4), 461–469, doi:10.1016/j.epsl.2011.05.027.
- Montési, L. G. J., and M. D. Behn (2007), Mantle flow and melting underneath oblique and ultraslow mid-ocean ridges, *Geophys. Res. Lett.*, *34*, L24307, doi:10.1029/2007GL031067.

- Nedimović, M. R., S. M. Carbotte, A. J. Harding, R. S. Detrick, J. P. Canales, J. B. Diebold, G. M. Kent, M. Tischer, and J. M. Babcock (2005), Frozen magma lenses below the oceanic crust, *Nature*, *436*, 1149–1152, doi:10.1038/nature03944.
- Nicolas, A., and A. Prinzhofer (1983), Cumulative or residual origin for the transition zone in ophiolites: Structural evidence, *J. Petrol.*, *24*(2), 188–206, doi:10.1093/petrology/24.2.188.
- Norrell, G. T. (1991), Lithospheric strength and rheological stratification at mid-ocean ridges, *J. Geol. Soc.*, *148*, 521–525, doi:10.1144/gsjgs.148.3.0521.
- Perfit, M. R., et al. (1996), Recent volcanism in the Siqueiros transform fault: Picritic basalts and implications for MORB magma genesis, *Earth Planet. Sci. Lett.*, *141*(1–4), 91–108, doi:10.1016/0012-821X(96)00052-0.
- Phipps Morgan, J. (1987), Melt migration beneath mid-ocean spreading centers, *Geophys. Res. Lett.*, *14*(12), 1238–1241, doi:10.1029/GL014i012p01238.
- Rabinowicz, M., A. Nicolas, and J. L. Vigneresse (1984), A rolling mill effect in the asthenosphere beneath oceanic spreading centers, *Earth Planet. Sci. Lett.*, *67*(1), 97–108, doi:10.1016/0012-821X(84)90042-6.
- Reid, I., and H. R. Jackson (1981), Oceanic spreading rate and crustal thickness, *Mar. Geophys. Res.*, *5*(2), 165–172, doi:10.1007/BF00163477.
- Roland, E., M. D. Behn, and G. Hirth (2010), Thermal-mechanical behavior of oceanic transform faults: Implications for the spatial distribution of seismicity, *Geochem. Geophys. Geosyst.*, *11*, Q07001, doi:10.1029/2010GC003034.
- Rommevaux-Jestin, C., C. Deplus, and P. Patriat (1997), Mantle Bouguer anomaly along an ultra slow-spreading ridge: Implications for accretionary processes and comparison with results from central Mid-Atlantic Ridge, *Mar. Geophys. Res.*, *19*(6), 481–403, doi:10.1023/A:1004269003009.
- Ryan, M. P., and J. Y. K. Blevins (1987), *The Viscosity of Synthetic and Natural Silicate Melts and Glasses at High Temperatures and 1 Bar (10⁵ Pascals) Pressure and at Higher Pressures*, U.S. Geol. Surv. Bull., *1764*, 563 pp.
- Sauter, D., P. Patriat, C. Rommevaux-Jestin, M. Cannat, A. Briais, and Gallieni Shipboard Scientific Party (2001), The Southwest Indian Ridge between 49° 15'E and 57°E: Focused accretion and magma redistribution, *Earth Planet. Sci. Lett.*, *192*(3), 303–317, doi:10.1016/S0012-821X(01)00455-1.
- Sauter, D., V. Mendel, C. Rommevaux-Jestin, L. M. Parson, H. Fujimoto, C. Mével, M. Cannat, and K. Tamaki (2004), Focused magmatism versus amagmatic spreading along the ultra-slow spreading Southwest Indian Ridge: Evidence from TOBI side scan sonar imagery, *Geochem. Geophys. Geosyst.*, *5*, Q10K09, doi:10.1029/2004GC000738.
- Scott, D. R., and D. J. Stevenson (1984), Magma solitons, *Geophys. Res. Lett.*, *11*(11), 1161–1164, doi:10.1029/GL011i011p01161.
- Seyler, M., M. J. Toplis, J.-P. Lorand, A. Luguet, and M. Cannat (2001), Clinopyroxene microtextures reveal incompletely extracted melts in abyssal peridotites, *Geology*, *29*(2), 155–158, doi:10.1130/0091-7613(2001)029<0155:CMRIEM>2.0.CO;2.
- Shaw, A. M., M. D. Behn, S. E. Humphris, R. A. Sohn, and P. M. Gregg (2010), Deep pooling of low degree melts and volatile fluxes at the 85°E segment of the Gakkel Ridge: Evidence from olivine-hosted melt inclusions and glasses, *Earth Planet. Sci. Lett.*, *289*(3–4), 311–322, doi:10.1016/j.epsl.2009.11.018.
- Sims, K. W. W., et al. (2002), Chemical and isotopic constraints on the generation and transport of magma beneath the East Pacific Rise, *Geochim. Cosmochim. Acta*, *66*(19), 3481–3504, doi:10.1016/S0016-7037(02)00909-2.
- Sims, K. W. W., et al. (2003), Aberrant youth: Chemical and isotopic constraints on the origin of off-axis lavas from the East Pacific Rise, 9 degrees–10 degrees N, *Geochem. Geophys. Geosyst.*, *4*(10), 8621, doi:10.1029/2002GC000443.
- Sinton, J. M., and R. S. Detrick (1992), Mid-ocean ridge magma chambers, *J. Geophys. Res.*, *97*, 197–216, doi:10.1029/91JB02508.
- Sleep, N. H. (1974), Segregation of magma from a mostly crystalline mush, *Geol. Soc. Am. Bull.*, *85*(8), 1225–1232, doi:10.1130/0016-7606(1974)85<1225:SOMFAM>2.0.CO;2.
- Sleep, N. H. (2000), Evolution of the mode of convection within terrestrial planets, *J. Geophys. Res.*, *105*, 17,563–17,578, doi:10.1029/2000JE001240.
- Sparks, D. W., and E. M. Parmentier (1991), Melt extraction from the mantle beneath spreading centers, *Earth Planet. Sci. Lett.*, *105*(4), 368–377, doi:10.1016/0012-821X(91)90178-K.
- Sparks, D. W., E. M. Parmentier, and J. Phipps Morgan (1993), Three-dimensional mantle convection beneath a segmented spreading center: Implications for along-axis variations in crustal thickness and gravity, *J. Geophys. Res.*, *98*, 21,977–21,995, doi:10.1029/93JB02397.
- Spiegelman, M. (1993), Physics of melt extraction: Theory, implications and applications, *Philos. Trans. R. Soc. A*, *345*, 23–41, doi:10.1098/rsta.1993.0002.
- Spiegelman, M., and D. P. McKenzie (1987), Simple 2-D models for melt extraction at mid-ocean ridges and island arcs, *Earth Planet. Sci. Lett.*, *83*(1–4), 137–152, doi:10.1016/0012-821X(87)90057-4.
- Spiegelman, M., P. B. Kelemen, and E. Aharonov (2001), Causes and consequences of flow organization during melt transport: The reaction infiltration instability in compactible media, *J. Geophys. Res.*, *106*, 2061–2077, doi:10.1029/2000JB900240.
- Standish, J. J. (2005), The influence of ridge geometry at the ultraslow-spreading Southwest Indian Ridge (9°–25°E): Basalt composition sensitivity to variations in source and process, Ph. D. thesis, Mass. Inst. of Technol., Cambridge.
- Standish, J. J., and K. W. W. Sims (2010), Young off-axis volcanism along the ultraslow-spreading Southwest Indian Ridge, *Nat. Geosci.*, *3*, 286–292, doi:10.1038/ngeo824.
- Standish, J. J., H. J. B. Dick, P. J. Michael, W. Melson, and T. O'Hearn (2008), MORB generation beneath the ultraslow spreading Southwest Indian Ridge (9°–25°E): Major element chemistry and the importance of process versus source, *Geochem. Geophys. Geosyst.*, *9*, Q05004, doi:10.1029/2008GC001959.
- Su, W., and W. R. Buck (1993), Buoyancy effects on mantle flow under mid-ocean ridges, *J. Geophys. Res.*, *98*, 12,191–12,205, doi:10.1029/93JB00994.
- Tackley, P. J. (2000), Self-consistent generation of tectonic plates in time-dependent, three-dimensional mantle convection simulations: 2. Strain weakening and asthenosphere, *Geochem. Geophys. Geosyst.*, *1*(8), 1026, doi:10.1029/2000GC000043.
- Toomey, D. R., W. S. D. Wilcock, S. C. Solomon, W. C. Hammond, and J. A. Orcutt (1998), Mantle seismic structure beneath the MELT region of the East Pacific Rise from P and S wave tomography, *Science*, *280*, 1224–1227, doi:10.1126/science.280.5367.1224.
- Tucholke, B. E., M. D. Behn, W. R. Buck, and J. Lin (2008), The role of melt supply in oceanic detachment faulting and formation of megamullions, *Geology*, *36*(6), 455–458, doi:10.1130/G24639A.
- von Bargen, N., and H. S. Waff (1986), Permeabilities, interfacial areas and curvatures of partially molten systems: Results of numerical computations of equilibrium microstructures, *J. Geophys. Res.*, *91*, 9261–9276, doi:10.1029/JB091iB09p09261.
- Warren, J. M., and N. Shimizu (2010), Cryptic variations in abyssal peridotite compositions: Evidence for shallow-level melt infiltration in the oceanic lithosphere, *J. Petrol.*, *51*(1–2), 395–423, doi:10.1093/petrology/egp096.
- Warren, J. M., N. Shimizu, C. Sakaguchi, H. J. B. Dick, and E. Nakamura (2009), An assessment of upper mantle heterogeneity based on abyssal peridotite isotopic compositions, *J. Geophys. Res.*, *114*, B12203, doi:10.1029/2008JB006186.
- Weatherley, S. M., and R. F. Katz (2010), Plate-driven mantle dynamics and global patterns of mid-ocean ridge bathymetry, *Geochem. Geophys. Geosyst.*, *11*, Q10003, doi:10.1029/2010GC003192.
- White, R. S., T. A. Minshull, M. J. Bickle, and C. J. Robinson (2001), Melt generation at very slow-spreading oceanic ridges: Constraints from geochemical and geophysical data, *J. Petrol.*, *42*(6), 1171–1196, doi:10.1093/petrology/42.6.1171.
- Yang, H. J., R. J. Kinzler, and T. L. Grove (1996), Experiments and models of anhydrous, basaltic olivine-plagioclase-augite saturated melts from 0.001 to 10 kbar, *Contrib. Mineral. Petrol.*, *124*(1), 1–18, doi:10.1007/s004100050169.
- Zhu, W., and G. Hirth (2003), A network model for permeability in partially molten rocks, *Earth Planet. Sci. Lett.*, *212*(3–4), 407–416, doi:10.1016/S0012-821X(03)00264-4.
- Zhu, W., G. A. Gaetani, F. Fusses, L. G. J. Montési, and F. De Carlo (2011), Microtomography of partially molten rocks: Three-dimensional melt distribution in mantle peridotite, *Science*, *332*, 88–91, doi:10.1126/science.1202221.

J. L. Barry, Computer Science and Artificial Intelligence Laboratory, Massachusetts Institute of Technology, Cambridge, MA 02139, USA.
 M. D. Behn and J. Lin, Department of Geology and Geophysics, Woods Hole Oceanographic Institution, Woods Hole, MA 02543, USA.
 L. B. Hebert and L. G. J. Montési, Department of Geology, University of Maryland, College Park, MD 20742, USA. (montesi@umd.edu)